

Omnigenous stellarator equilibria with enhanced stability

R. Gaur, R. Conlin, D. Dickinson, J. F. Parisi, D. Dudt, D. Panici, P. Kim, K. Unalmis, W. D. Dorland, E. Kolemen

Department of Mechanical and Aerospace Engineering, Princeton University,
Princeton, New Jersey, USA

Princeton Plasma Physics Laboratory, Princeton, New Jersey, USA

School of Physics, Engineering, and Technology, University of York, Heslington,
York, UK

Thea Energy

IREAP, University of Maryland, College Park, USA

Department of Physics, University of Maryland, College Park, USA

E-mail: rg6256@princeton.edu, rgaur@terpmail.umd.edu

October 2024

Abstract. To build an economically viable stellarator, it is essential to find a configuration that satisfies a set of favorable properties to achieve efficient steady-state nuclear fusion. One such property is omnigenity, which ensures confinement of trapped particles. After creating an omnigenous equilibrium, one must also ensure reduced transport resulting from kinetic and magnetohydrodynamic (MHD) instabilities. This study introduces and leverages the GPU-accelerated DESC optimization suite, which is used to design stable high- β omnigenous equilibria, achieving Mercier, ideal ballooning, and enhanced kinetic ballooning stability. We explain the link between ideal and kinetic ballooning modes and discover stellarators with second stability, a regime of large pressure gradient where an equilibria becomes ideal ballooning stable.

Keywords: stellarator, optimization, stability, turbulence

1. Introduction

Stellarators [1] are toroidal devices that are used for magnetic confinement of a hot plasma to achieve nuclear fusion. Unlike their toroidally axisymmetric counterparts, tokamaks, stellarators can provide a greater range of design flexibility that is used to improve their operational properties. The lack of toroidal symmetry also allows us to twist the magnetic field by shaping the boundary, thereby reducing the net toroidal current and avoiding current-driven plasma instabilities and disruptions. However, finding the optimal stellarator design from a large design space with hundreds of millions of possible configurations can become a complicated optimization problem.

Previous-generation optimizers such as STELLOPT [2], ROSE [3], and SIMSOPT [4] use the VMEC [5] code, a three-dimensional ideal magnetohydrodynamics (MHD) equilibrium solver. Using equilibrium data from VMEC, these optimizers calculate gradients of various quantities of interest using finite-difference techniques. However, the use of these techniques introduces noise into the gradient calculation. There has also been significant progress in improving the speed and accuracy of these gradients using adjoint methods [6]. But these techniques still depend on equilibrium dependent gradients, must be customized to each objective, and do not work for highly-nonlinear chaotic problems. It has also been shown [7] that the VMEC equilibria can be inaccurate near the magnetic axis because they do not satisfy the ideal MHD force balance equation.

To this end, we have developed the DESC stellarator [7–10] equilibrium and optimization suite. Using the DESC optimizer, we can calculate and optimize stellarator equilibria with favorable properties such as omnigenity, MHD stability, low neoclassical transport, and coil shape complexity while ensuring ideal MHD force balance throughout the device volume. In this paper, we will demonstrate the utility of the DESC code by optimizing equilibria for various stability properties, with a focus on a gyrokinetic instability known as the Kinetic Ballooning Mode (KBM).

In this paper, we will focus on high- β stellarators, where $\beta = 2\mu_0 p/B^2$ is the ratio of plasma pressure to magnetic pressure. Low-beta stellarators are typically dominated by electrostatic instabilities such as the ion temperature gradient (ITG) mode [11, 12] and trapped electron mode (TEM) [13, 14], which drive the most high heat and particle losses, degrading the performance of reactors. However, at high- β , the electrostatic modes become subdominant, and electromagnetic instabilities can become a problem. In particular, much work in the literature discusses how a long-wavelength gyrokinetic instability, known as the Kinetic Ballooning Mode (KBM) [15], can potentially cause huge heat and particle losses as a result of turbulent transport. Therefore, reducing the susceptibility of high- β stellarators to the KBM is paramount.

We develop a set of omnigenous high- β stellarator equilibria with enhanced KBM stability. In Section 2, we briefly explain the steady-state ideal MHD model and how we can locally vary the gradients associated with an equilibrium to gain insight into the stability properties of an equilibrium. In Section 3, we introduce the linear gyrokinetic model and discuss the limit in which it reduces to the infinite- n ideal ballooning equation. We test our hypothesis by analyzing a high-beta W7X equilibrium and demonstrating a strong correlation between the ideal and kinetic ballooning modes. In Section 4, we explain the details of the reverse-mode-differentiable ideal ballooning solver implemented in DESC. In Section 5, we explain how we calculate omnigenous equilibria in DESC. In Section 6, we obtain and present three stellarator configurations with poloidal, toroidal, and helical omnigenity, respectively. We explain the objective functions used to calculate these equilibria and analyze their physical properties, such as KBM stability. In Section 7, we conclude our work and discuss various directions in which it can be extended.

2. Ideal MHD equilibrium

In this section, we briefly explain how we define and calculate an ideal MHD equilibrium in a stellarator. We then explain how to locally vary the gradients of that equilibrium.

A divergence-free magnetic field \mathbf{B} can be written in the Clebsch form [16]

$$\mathbf{B} = \nabla\psi \times \nabla\alpha, \quad (1)$$

We will focus on solutions whose magnetic field lines lie on closed nested toroidal surfaces, known as flux surfaces. We label these surfaces using the enclosed toroidal flux ψ . On each flux surface, the lines of constant α coincide with the magnetic field lines. Thus, α is known as the field line label. We define $\alpha = \theta - \iota(\zeta - \zeta_0)$, where θ is the PEST straight field line angle, ζ is the cylindrical toroidal angle, ζ_0 is a constant, and

$$\iota = \frac{\mathbf{B} \cdot \nabla\theta}{\mathbf{B} \cdot \nabla\zeta}, \quad (2)$$

is the pitch of the magnetic field lines on a flux surface, known as the rotational transform. Using the Clebsch form of the magnetic field, we solve the ideal MHD force balance equation

$$\mathbf{j} \times \mathbf{B} = \nabla p, \quad (3)$$

where the plasma current $\mathbf{j} = (\nabla \times \mathbf{B})/\mu_0$ from Ampere's law, p is the plasma pressure and μ_0 is the vacuum magnetic permeability. Unlike an axisymmetric case, for stellarators, we have to solve (3) as an optimization problem. We achieve this with the DESC [7–10] stellarator optimization suite. DESC can simultaneously solve an equilibrium while optimizing for multiple objectives such as MHD stability, quasisymmetry, and many more. In this paper, we use some of these metric to generate various stellarator equilibria. The details of the DESC package are briefly provided in Appendix A. In the following sections, we explain how to utilize DESC to optimize stellarator equilibria for various favorable properties.

2.1. Locally varying the gradients of pressure and rotational transform

In this section, we will briefly explain the method of local equilibrium variation and how we use it to analyze stability in stellarators.

To better understand the stability property of stellarator equilibria, we can locally vary the gradients of the pressure and rotational transform and obtain a family of local equilibria that are in ideal MHD force balance. We then analyze the stability properties of these equilibria. This gives us an idea of how these equilibria would behave if the pressure and rotational transform profiles were modified. This type of analysis is also known as a \hat{s} - α_{MHD} analysis. According to convention, we normalize the gradients to two parameters: the magnetic shear

$$\hat{s} = -\frac{\rho}{\iota} \frac{d\iota}{d\rho}, \quad (4)$$

and the normalized pressure gradient

$$\alpha_{\text{MHD}} = -\frac{1}{B_N^2} \frac{dp}{d\rho}, \quad (5)$$

respectively, where $\rho = \sqrt{\psi/\psi_b}$ is the normalized radius, $B_N = 2\psi_b/(\pi a_N^2)$ and $a_N = \sqrt{A/\pi}$ is the effective minor radius, and A is toroidally-averaged cross-section area. In the context of stability, the $\hat{s} - \alpha_{\text{MHD}}$ analysis has been used in both tokamaks [17] and stellarators [18, 19]. The details and formulation of an $\hat{s} - \alpha_{\text{MHD}}$ analysis with DESC is described in Appendix C.

Note that the idea of locally varying the gradients of an equilibrium is only applicable to instabilities that are localized to a flux surface. In this work, we apply this technique to the infinite- n ideal ballooning mode and the δf gyrokinetic model, both of which are models used to study small-scale instabilities localized to a flux surface.

Using the method of local equilibrium variation with the DESC, we will vary the gradients \hat{s} and α_{MHD} on different flux surfaces and scan the MHD stability of a family of equilibria. Using this technique, in the next section, we will analyze the kinetic stability of the same equilibria with the gyrokinetic solver GS2 and explain the relation between the KBM and the infinite- n , ideal ballooning mode.

3. Analyzing local ideal MHD and gyrokinetic stability in stellarators

In this section, we introduce the linear δf gyrokinetic model, explain the limit in which it can be simplified to obtain the KBM equations, and demonstrate how the KBM may be related to the infinite- n ideal ballooning mode. We further explore this theoretical connection by numerically solving linear gyrokinetic equations using the GS2 code and performing a scan of the maximum KBM growth rate by locally varying the pressure gradient and rotational transform for a typical equilibrium for the W7-X stellarator.

We take the linearized, δf gyrokinetic model from Abel *et al.* [20–22] and write a simplified set of equations describing the evolution of the gyrokinetic distribution function in the guiding-center coordinate system $(\mathbf{R}_s, E_s, \mu_s, t)$

$$h_s(\mathbf{R}_s, E_s, \mu_s, t) = \frac{Z_s e \varphi(\mathbf{r}, t) F_{0s}}{T_s} + \delta f_s(\mathbf{R}_s, E_s, \mu_s, t), \quad (6)$$

the fluctuations of the electrostatic potential φ , parallel component δA_{\parallel} of the magnetic vector potential, and the parallel fluctuation of the magnetic field strength $\delta B_{\parallel} = \mathbf{b} \cdot (\nabla \times \delta \mathbf{A}_{\perp})$. The full set of simplified, linear equations

$$\frac{\partial h_s}{\partial t} + (w_{\parallel} \mathbf{b} + \mathbf{v}_{Ds}) \cdot \frac{\partial h_s}{\partial \mathbf{R}_s} = \frac{Z_s e F_{0s}}{T_s} \frac{\partial \langle \varphi - \mathbf{w} \cdot \delta \mathbf{A} / c \rangle_{\mathbf{R}_s}}{\partial t} - \mathbf{V}_E \cdot \nabla F_{0s}, \quad (7)$$

$$\sum_s \frac{(Z_s e)^2 \varphi}{T_s} = \sum_s Z_s e \int d^3 \mathbf{w} \langle h_s \rangle_{\mathbf{r}}, \quad \tau = \frac{T_e}{T_i}, \quad (8)$$

$$-\nabla_{\perp}^2 \delta A_{\parallel} = \frac{4\pi}{c} \sum_s Z_s e \int d^3 \mathbf{w} w_{\parallel} \langle h_s \rangle_{\mathbf{r}}, \quad (9)$$

$$\nabla_{\perp}^2 \frac{\delta B_{\parallel} B}{4\pi} = -\nabla_{\perp} \nabla_{\perp} : \sum_s \int d^3 \mathbf{w} \langle m_s \mathbf{w}_{\perp} \mathbf{w}_{\perp} h_s \rangle_{\mathbf{r}}, \quad (10)$$

where \mathbf{v}_{Ds} is the magnetic drift velocity and \mathbf{V}_E is the $\mathbf{E} \times \mathbf{B}$ velocity defined as

$$\mathbf{v}_{Ds} = \frac{w_{\parallel}^2}{\Omega_s} \mathbf{b} \times (\mathbf{b} \cdot \nabla \mathbf{b}) + \frac{w_{\perp}^2}{2\Omega_s} \frac{\mathbf{b} \times \nabla B}{B}, \quad (11)$$

$$\mathbf{V}_E = \frac{c}{B} \mathbf{b} \times \langle \nabla \varphi \rangle_{\mathbf{R}_s} - \frac{1}{B} \mathbf{b} \times \langle \nabla (\mathbf{w} \cdot \delta \mathbf{A}) \rangle_{\mathbf{R}_s}, \quad (12)$$

and the subscript s is used to define these quantities for different species. The gyrofrequency of a species is $\Omega_s = Z_s e B / (m_s c)$, Z_s being the charge of the species. For this study, we choose a hydrogen plasma made of ions and electrons, with $Z_i = 1$, $Z_e = -1$. Both species have the same temperature, which corresponds to $\tau = 1$.

To simplify the model further, we use a normal model ansatz where all the fluctuating quantities are assumed to be periodic perpendicular to the field line. This allows us to write the fluctuating quantities as a Fourier series.

$$h_s = \exp(i\omega t) \sum_k h_{k_{\perp},s}(\zeta, E_s, \lambda, \sigma, t) \exp(i\mathbf{k}_{\perp} \cdot \mathbf{R}_s), \quad (13a)$$

$$\varphi = \exp(i\omega t) \sum_k \varphi_{k_{\perp}}(\zeta, t) \exp(i\mathbf{k}_{\perp} \cdot \mathbf{r}), \quad (13b)$$

$$\delta A_{\parallel} = \exp(i\omega t) \sum_k \delta A_{\parallel,k_{\perp}}(\zeta, t) \exp(i\mathbf{k}_{\perp} \cdot \mathbf{r}), \quad (13c)$$

$$\delta B_{\parallel} = \exp(i\omega t) \sum_k \delta B_{\parallel,k_{\perp}}(\zeta, t) \exp(i\mathbf{k}_{\perp} \cdot \mathbf{r}), \quad (13d)$$

where ω is the complex frequency of the mode, $E_s = m_s w^2 / 2$, is the particle energy, $\mu_s = m_s w_{\perp}^2 / (2B)$ is its magnetic moment, $\lambda = \mu / E$ is the pitch angle, and $\sigma = w_{\parallel} / |w_{\parallel}|$ is the streaming direction of a particle. Using this ansatz and dropping the subscript k_{\perp} , we can rewrite the linearized δf gyrokinetic model

$$\begin{aligned} i(\omega - \omega_{Ds}) h_s + (\mathbf{b} \cdot \nabla \zeta) w_{\parallel} \frac{\partial h_s}{\partial \zeta} \\ = (\omega - \omega_{*,s}^T) \left[J_0 \left(\frac{k_{\perp} w_{\perp}}{\Omega_s} \right) \left(\varphi - \frac{w_{\parallel} \delta A_{\parallel}}{c} \right) + J_1 \left(\frac{k_{\perp} w_{\perp}}{\Omega_s} \right) \frac{w_{\perp}}{k_{\perp}} \frac{\delta B_{\parallel}}{c} \right] F_{0s}, \end{aligned} \quad (14)$$

$$\sum_s \frac{q_s^2 N_s \delta \varphi}{T_s} = \sum_s q_s \int d^3 \mathbf{v} J_{0s} h_s, \quad (15)$$

$$k_{\perp}^2 \delta A_{\parallel} = \sum_s \frac{4\pi q_s}{c} \int d^3 \mathbf{v} v_{\parallel} J_{0s} h_s, \quad (16)$$

$$\frac{B}{4\pi} \delta B_{\parallel} = - \sum_s \int d^3 \mathbf{v} v_{\perp}^2 \frac{m_s J_{1s} \Omega_s}{k_{\perp} v_{\perp}} h_s. \quad (17)$$

Here,

$$\omega_{Ds} = \mathbf{k}_{\perp} \cdot \mathbf{v}_{Ds}, \quad (18)$$

is the magnetic drift frequency, and $J_0(k_\perp \rho_s)$ and $J_1(k_\perp \rho_s)$ are the zeroth- and first-order cylindrical Bessel functions, respectively,

$$\frac{a_N}{L_{T_s}} = -\frac{d \log(T_s)}{d\rho}, \quad \frac{a_N}{L_{n_s}} = -\frac{d \log(n_s)}{d\rho}, \quad \eta_s = \frac{L_{n_s}}{L_{T_s}}, \quad (19)$$

$\rho = \sqrt{s} = \sqrt{\psi/\psi_b}$. The instability driving term

$$\omega_{*,s}^T = \omega_{*,s} \left[1 + \eta_s \left(\frac{E_s}{T_s} - \frac{3}{2} \right) \right], \quad (20)$$

where

$$\omega_{*,s} = \frac{T_s}{Z_s e B} [(\mathbf{b} \times \mathbf{k}_\perp) \cdot \nabla \log n_s]. \quad (21)$$

is the diamagnetic drift frequency. We have now fully defined the linear gyrokinetic system as an eigenvalue problem. These equations can be further simplified under appropriate limits as described in Appendix C to obtain the infinite- n ideal ballooning equation,

$$\mathbf{B} \cdot \nabla \left(\frac{|\nabla \alpha|^2}{B^2} \mathbf{B} \cdot \nabla \hat{X} \right) + 2 \frac{dp}{d\psi} [\mathbf{B} \times (\mathbf{b} \cdot \nabla \mathbf{b})] \cdot \nabla \alpha \hat{X} = \lambda \frac{|\nabla \alpha|^2}{B^2} \hat{X}, \quad \lambda = -\frac{a_N^2}{v_A^2} \omega^2 \quad (22)$$

where \hat{X} is the eigenfunction and ω is the complex frequency of the KBM, and $v_A = B_N/\sqrt{4\pi\rho_0}$ is the Alfvén speed and a_N is the effective minor radius defined in section 2.1 subject to the boundary conditions

$$\lim_{\zeta \rightarrow \pm\infty} X(\theta) = 0 \quad (23)$$

where λ is the eigenvalue and \hat{X} is the eigenfunction. An equilibrium with $\lambda > 0$ implies an unstable mode, while $\lambda < 0$ implies stability. For each flux surface, equation (22) is solved on multiple field lines α for multiple values of the ballooning parameter ζ_0 . For each surface, we choose the maximum λ from the $\alpha - \zeta_0$ grid.

The ideal ballooning mode is closely related to the KBM in the large aspect ratio, high- β ordering. Hence, we can use the ideal ballooning mode to predict the behavior of the kinetic ballooning mode and optimize stellarators for linear ideal and kinetic ballooning instabilities.

3.1. Distance from ideal ballooning marginality as a proxy for KBM stability

To demonstrate the connection between the ideal and kinetic ballooning modes, we perform a $\hat{s} - \alpha_{\text{MHD}}$ analysis for a high- β W7-X equilibrium by numerically solving the linear gyrokinetic equation using the GS2 [23–26] solver and present our results in Figure 1. We vary \hat{s} and α_{MHD} of the equilibrium on four flux surfaces and, for each pair of values, calculate the maximum KBM growth rate in the $\hat{s} - \alpha_{\text{MHD}}$ space. We then compare it with the ideal ballooning stable and unstable regions in $\hat{s} - \alpha_{\text{MHD}}$ space. The details of these gyrokinetic calculations and the process used to extract maximum KBM growth rate is explained in Appendix E

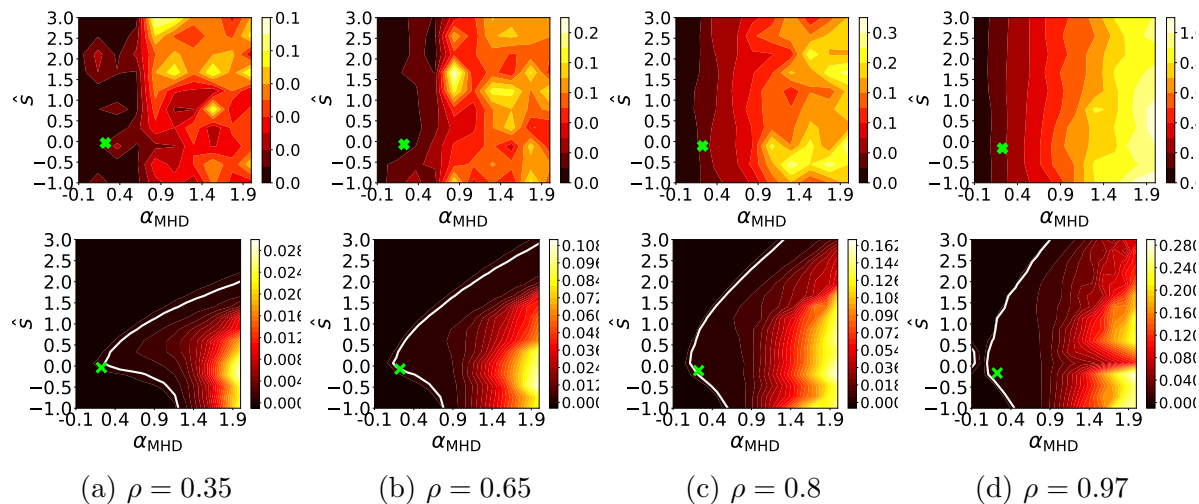


Figure 1: We present a $\hat{s} - \alpha_{\text{MHD}}$ calculation of the maximum KBM growth rate (top row) and the ideal ballooning growth rate (bottom row) on four flux surfaces from core (left) to edge (right) of a W7-X stellarator equilibrium. The crosses mark the original values of \hat{s} and α_{MHD} whereas the white line is the marginal stability contour. The region enclosed by the contour is ballooning unstable and the region outside is ballooning stable. There is a strong correlation between the ideal-ballooning unstable region and the regions with a high KBM growth rate, that we shall use to optimize equilibria against KBMs.

The most important feature in Figure 1 is the strong correlation between the ideal and kinetic ballooning modes. We observe that the KBM growth rate decreases as we move farther away left (outside) of the contour of marginal stability. Hence, the distance from ideal-ballooning marginal stability can be used as a proxy for improving KBM stability. Increasing the distance from ideal-ballooning marginal stability is equivalent to obtaining equilibria with a large negative λ .

The second point concerns the stability against the ballooning mode at large α_{MHD} . In tokamaks, increasing the pressure gradient can make the equilibrium stable against the ideal ballooning as explained by figure 2. This is equivalent to the green crosses in figure 1 moving from stable to unstable and back to stable regions. This stable region corresponding to large values of α_{MHD} is called the second stability region. However, second stability generally does not exist in stellarator as has been shown by Hegna and Hudson [27]. From Figure 1, for the range of \hat{s} and α_{MHD} it is clear that for this W7X configuration, a region of second stability does not exist at any radius.

4. Reverse-mode-differentiable infinite- n ideal ballooning solver in DESC

In this section, we briefly explain the ballooning solver implemented in the DESC optimizer and how we leverage automatic differentiation to speed up the gradient calculation. We also benchmark our solver against existing solvers.

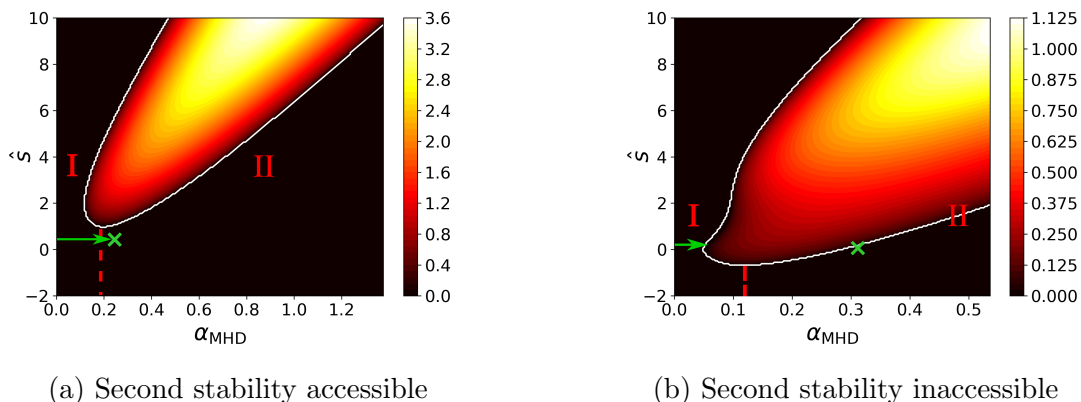


Figure 2: $\hat{s} - \alpha_{\text{MHD}}$ diagram plotting the ideal ballooning growth rate, taken from figure 5(e)(left) and 6(c)(right) of Gaur *et al* [28] for a modified DIII-D-like tokamak equilibrium. The dotted red line marks the region between the first stability (marked as I) and the second stability (marked as II). The cross marks the nominal gradient on the flux surface. The green arrow marks the path that an equilibrium may take to access that state starting from a vacuum state. In contrast to tokamaks, stellarators, in general, do not exhibit a second-stable region or a potential path to such a region as shown in figure 1.

Extending the work in [29], we develop a reverse-mode differentiable, fast, and accurate solver for the infinite- n ideal ballooning equation in DESC. In a package that facilitates automatic differentiation, reverse mode gradients allow us to calculate gradients of physical quantities, which in this case is the maximum eigenvalue λ_{max} in (27), by automatically applying the chain rule between the final quantity and the input parameters of the problem \mathbf{p} . This speeds up the calculation $\partial\lambda/\partial\mathbf{p}$ compared to the forward-mode gradient calculation by a factor of the number of parameters $N_{\mathbf{p}}$, similar to an adjoint method. However, we can obtain reverse mode gradients without solving an adjoint equation and using explicit formulae as used in [29]. In that sense, this technique is much more modular and powerful than adjoint methods.‡

To solve the infinite- n ideal ballooning equation, we discretize (22) along a field line α using the finite-difference scheme described in [30]

$$g_{j+1/2} \frac{(\hat{X}_{j+1} - \hat{X}_j)}{\Delta\zeta^2} - g_{j-1/2} \frac{(\hat{X}_j - \hat{X}_{j-1})}{\Delta\zeta^2} + (c_j - \hat{\lambda}f_j)\hat{X}_j = 0, \quad j = 0 \dots N-1, \quad (24)$$

where

$$g = (\mathbf{b} \cdot \nabla\zeta) \frac{|\nabla\alpha|^2}{B}, \quad (25a)$$

$$c = \frac{1}{B^2} \frac{d(\mu_0 p)}{d\psi} \frac{2}{(\mathbf{b} \cdot \nabla\zeta)} (\mathbf{b} \times \boldsymbol{\kappa}) \cdot \nabla\alpha, \quad \boldsymbol{\kappa} = (\mathbf{b} \cdot \nabla\mathbf{b}) \quad (25b)$$

‡ One has to carefully define these types of problems in DESC as not all objectives are reverse-mode differentiable. This is especially true for objectives involving time-dependent nonlinear dynamics.

$$f = \frac{1}{(\mathbf{b} \cdot \nabla \zeta)} \frac{|\nabla \alpha|^2}{B^3}, \quad (25c)$$

calculated on a uniformly-spaced grid with points being separated by $\Delta\zeta$, subject to the boundary conditions

$$\widehat{X}_0 = 0, \widehat{X}_N = 0. \quad (26)$$

The discretized eigenvalue equation can be written as

$$\mathcal{A}X = \lambda\mathcal{B}X \quad (27)$$

where \mathcal{A} is symmetric, tridiagonal matrix

$$\mathcal{A} = \begin{bmatrix} \frac{g_{1/2} + g_{3/2} - (\Delta\zeta)^2 c_1}{(\Delta\zeta)^2} & -\frac{g_{3/2}}{(\Delta\zeta)^2} & 0 & 0 & \dots & 0 & 0 \\ -\frac{g_{3/2}}{(\Delta\zeta)^2} & \frac{g_{3/2} + g_{5/2} - (\Delta\zeta)^2 c_2}{(\Delta\zeta)^2} & -\frac{g_{5/2}}{(\Delta\zeta)^2} & 0 & \dots & 0 & 0 \\ & & \ddots & & & & \\ & & & \ddots & & & \\ 0 & 0 & 0 & 0 & \dots & \frac{g_{N-5/2} + g_{N-3/2} - (\Delta\zeta)^2 c_{N-2}}{(\Delta\zeta)^2} & -\frac{g_{N-3/2}}{(\Delta\zeta)^2} \\ 0 & 0 & 0 & 0 & \dots & -\frac{g_{N-3/2}}{(\Delta\zeta)^2} & \frac{g_{N-3/2} + g_{N-1/2} - (\Delta\zeta)^2 c_{N-1}}{(\Delta\zeta)^2} \end{bmatrix}$$

and \mathcal{B} is a symmetric, diagonal matrix

$$\mathcal{B} = \begin{bmatrix} f_1 & 0 & 0 & 0 & \dots & 0 & 0 \\ 0 & f_2 & 0 & 0 & \dots & 0 & 0 \\ & & \ddots & & & & \\ & & & \ddots & & & \\ 0 & 0 & 0 & 0 & \dots & f_{N-2} & 0 \\ 0 & 0 & 0 & 0 & \dots & 0 & f_{N-1} \end{bmatrix}$$

Using DESC, we solve (27) on $N_\rho = 6$ flux surfaces with $\rho \in [0.15, 0.95]$. On each flux surface, we solve the ballooning equation on the $N_\alpha = 14$ field lines with $\alpha \in [0, \pi]$ and for $N_{\zeta_0} = 15$ values of the ballooning parameter $\zeta_0 \in [-\pi/2, \pi/2]$ to find the maximum eigenvalue $\lambda_{\max} = \max(\lambda_{j,k}) \forall j \in [1, N_{\zeta_0}], k \in [1, N_\alpha], j, k \in \mathbb{Z}$. Using this definition, we define the following ballooning objective function for each flux surface

$$f_{\text{ball},i} = w_0 \text{ReLU}(\lambda_{\max} - \lambda_0) + w_1 \sum_{j=1}^{N_{\zeta_0}} \sum_{k=1}^{N_\alpha} \text{ReLU}(\lambda_{j,k} - \lambda_0) \quad (28)$$

where ReLU is the Rectified Linear Unit operator, i is the index of the flux surface, w_0, w_1 are constant weights, and $\lambda_0 < 0$ is the desired distance from ideal-ballooning marginality.

As a benchmark, we present a comparison of our ideal ballooning solver with COBRAVMEC [30] and a convergence study with equilibrium resolution in Figure 3.

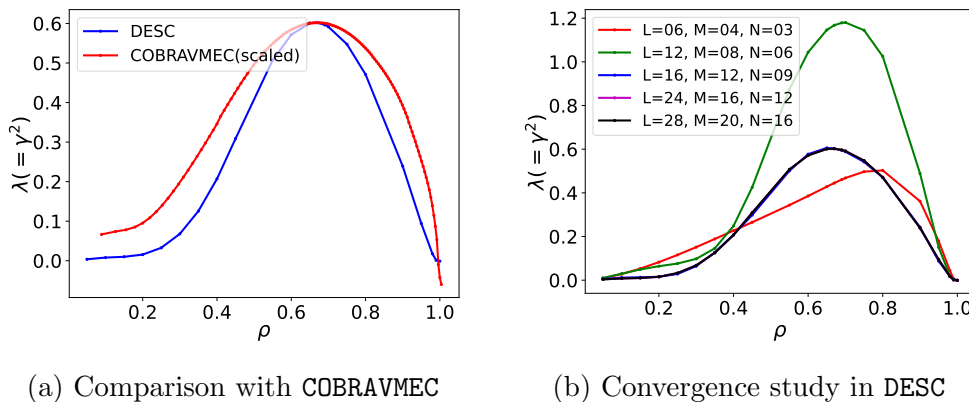


Figure 3: Comparison of the DESC ballooning solver with COBRAVMEC shown in (a). Due to different normalizations, the COBRAVMEC output has been scaled by the ratio $\lambda_{\max, \text{DESC}} / \lambda_{\max, \text{COBRAVMEC}}$. In (b), we show a convergence test of the maximum ballooning eigenvalue with increasing equilibrium resolution L, M, N . To calculate λ_{\max} , we scan over $N_\alpha = 14$ field lines, and $N_{\zeta_0} = 15$ values of the ballooning parameter $\zeta_0 \in [-\pi/2, \pi/2]$. On each field line, we choose $N_0 = 8 \times 1.5M \times 1.5N$ points with $\zeta \in [-4\pi, 4\pi]$, where M, N are the poloidal and toroidal resolution of a DESC equilibrium, respectively. Since the pressure gradient $dp/d\psi = 0$ on the magnetic axis for this equilibrium, $\lambda_{\max} \leq 0$ which is satisfied by the DESC solver.

5. Omnigenity

Omnigenity is a favorable property of a magnetic field that ensures the radial confinement of the trapped particles in a stellarator. Mathematically, an ideal MHD equilibrium with nested flux surfaces is omnigenous [31] if

$$\int_{\zeta_{b1}}^{\zeta_{b2}} \frac{d\zeta}{(\mathbf{b} \cdot \nabla \zeta)} (\mathbf{v}_{D_s} \cdot \nabla \psi) = 0 \quad (29)$$

where the particle drift \mathbf{v}_{D_s} is the magnetic drift velocity, defined in (11), ζ is a field-line following coordinate, ζ_{b1} and ζ_{b2} are the bounce points of a particle and the integral operation, known as bounce-averaging, denotes the average radial deviation of a particle from a flux surface. For a system with a longitudinal adiabatic invariant,

$$J_{\parallel} = \int_{\zeta_{b1}}^{\zeta_{b2}} \frac{d\zeta}{(\mathbf{b} \cdot \nabla \zeta)} w_{\parallel}, \quad (30)$$

the omnigenity condition is equivalent to $\partial_\alpha J_{\parallel} = 0$ implying that the longitudinal adiabatic invariant is a flux function for omnigenous equilibria.

Due to axisymmetry, a continuous toroidal symmetry, tokamaks are inherently omnigenous. Since stellarators do not possess continuous toroidal symmetry, they have to be optimized for omnigenity. Most of the work over the last decade in stellarator optimization has focused on a subset of omnigenity, a hidden symmetry known as quasisymmetry [32]. For quasi-symmetric equilibria, the magnetic field strength B on

a flux surface can be completely defined by a single angular coordinate unlike a general stellarator magnetic field $B = B(\theta, \zeta)$ that requires two angular coordinates.

Depending on the topology of the magnetic field, a quasisymmetric configuration can have $B = B(\theta_B)$, $B = B(\theta_B - n_{\text{FP}}\zeta_B)$, or $B = B(\zeta_B)$, where θ_B, ζ_B are Boozer angles, and n_{FP} is the field period, a positive integer characterizing the discrete toroidal symmetry of a stellarator. In the same order as defined in the previous sentence, these equilibria are called quasiaxisymmetric (QA), quasihelically symmetric (QH), and quasipoloidally symmetric (QP). Analogous to quasisymmetry, Cary and Shasharina [33] developed a specialized angular coordinate system in which one can define omnigenity in terms of the magnetic field strength in a manner analogous to quasisymmetry. Since omnigenity is a superset of quasisymmetry, it expands the space of possible omnigenous configurations, allowing us to optimize for additional favorable properties, apart from omnigenity. In this work, we optimize stellarators for equilibria with poloidal omnigenity (OP), toroidal omnigenity (OT), and helical omnigenity (OH) along with additional objectives related to MHD and kinetic stability.

In recent years, there have been many stellarator designs with poloidal omnigenity OP (also known as QI) [34–37] but toroidal or helical omnigenity has not been explored. In this work, we use the Cary and Shasharina’s [38] technique and numerically implemented by Dudt *et al.* [10] in the DESC code to find omnigenous stellarator configurations. The theory and implementation are briefly described in the following paragraphs.

Cary and Shasharina derived the following conditions that an omnigenous field must satisfy on each flux surface:

- (i) The minimum and maximum magnetic field strength B_{\min} and B_{\max} must be independent of the field line label α
- (ii) The contour of the maximum magnetic field strength must be a straight line in Boozer coordinates

To satisfy these conditions, they define the magnetic field strength in a coordinate system $B = B(\rho, \eta)$, where η is a specialized angular coordinate and $B(\eta = 0) = B_{\min}$ and $B(\eta = \pm\pi/2) = B_{\max}$.

To implement these omnigenous target magnetic fields, Dudt *et al.* [10] design a target omnigenous field profile $B(\rho, \eta)$ and a transformation that transforms the target magnetic field from the computational angular coordinates (η, α) to Boozer coordinates (θ_B, ζ_B) on each flux surface. Transformation $h : (\rho, \theta_B, \zeta_B) \rightarrow (\rho, \eta, \alpha)$ is defined as

$$h = 2\eta + \pi + \sum_{l=0}^{L_\rho} \sum_{m=0}^{M_\eta} \sum_{n=-N_\alpha}^{N_\alpha} x_{lmn} T_l(2\rho - 1) F_m(\eta) F_{nn_{\text{FP}}}(\alpha), \quad l \in \mathbb{Z} \quad (31)$$

where the terms T_l are the Chebyshev polynomial of first kind, and

$$F_k = \begin{cases} \cos(|k|y) & \text{for } k \geq 0 \\ \sin(|k|y) & \text{for } k < 0 \end{cases} \quad (32)$$

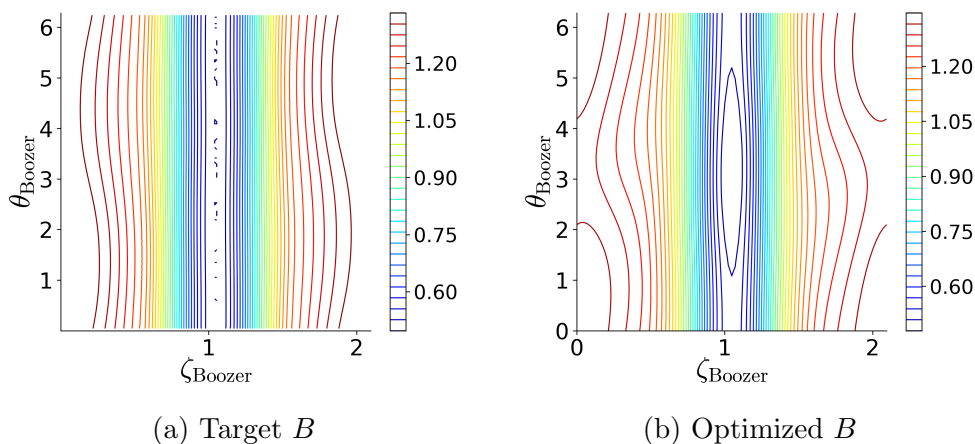


Figure 4: Comparison of a typical poloidally omnigenous magnetic field (in Boozer coordinates) on the flux surface for an optimized configuration. Figure (a) shows the target omnigenous field generated using the Cary-Shasharina prescription, whereas (b) shows the optimized equilibrium field.

are the Fourier modes corresponding to the η and α coordinates, L_ρ, M_η, N_α are the resolutions of the each coordinate transformation, and x_{lmn} are the spectral coefficients. To impose the condition (ii) related to the B_{\max} contours, we also have to impose the linear constraint

$$\sum_{m=0,2,4,\dots}^{M_\eta} (-1)^{\frac{m}{2}+1} x_{lmn} = 0. \quad (33)$$

For each optimization step, to improve the omnigenity of the equilibrium, DESC penalizes the equilibrium field B_{eq} through the objective

$$f_{\text{om}} = \sum_i (B_{\text{eq},i} - B)^2, \quad (34)$$

where B is the target omnigenous field and i is the index of the flux surface over which f_{om} is calculated. By minimizing f_{om} over multiple flux surfaces, we ensure that the equilibrium field is as close to omnigenous as possible §. A typical example showing the equilibrium and target omnigenous field is presented in Figure 4.

6. Omnigenous equilibria with enhanced KBM stability

In this section, we explain how we generate omnigenous equilibria with improved stability with DESC. Using the ideas explained in the previous sections, we first search for omnigenous stellarators with poloidally closed contours. To do that, we use the following objective function

$$\mathcal{F} = \mathbf{A}f_{\text{aspect}}^2 + \mathbf{B}f_{\text{ball}}^2 + \mathbf{C}f_{\text{curv}}^2 + \mathbf{D}f_{\text{DMerc}}^2 + \mathbf{E}f_{\text{elongation}}^2 + \mathbf{O}f_{\text{om}}^2, \quad (35)$$

§ Note that minimizing f_{om} is a sufficient but not a necessary condition to ensure omnigenity. An equilibrium field could deviate significantly from the target field B , *i.e.*, have a large f_{om} and still be omnigenous

where f_x are various objectives on the right side for omnigenity, distance from ideal-ballooning marginality, Mercier stability, boundary curvature, boundary elongation, and aspect ratio and A, B, C, D, E, O are weights used with each objective function. At each iteration of a DESC optimization, \mathcal{F} is minimized while satisfying (3). The exact definitions of these objectives are provided in Appendix D.

With the objective function defined, we run DESC on a single NVIDIA A100 GPU. A single optimization takes less than four hours. Currently, the speed of optimization is limited by the Boozer transformation needed for the omnigenity objective and the ideal-ballooning growth rate calculation. We expect a significant speedup as we vectorize these calculations and move towards DESC *v1.0*.

6.1. Poloidal omnigenity (OP)

Our objective is to find a poloidally omnigenous (OP) equilibrium with improved stability using DESC. Implementing the heuristic analytical model provided by Goodman et al. [35] and using the DESC omnigenity module, we have generated a database of 10^5 omnigenous equilibria [39]. From this database, we select a finite- β equilibrium with $n_{\text{FP}} = 3$, a low omnigenity error, and negative magnetic shear. We then optimize this equilibrium for improved stability using DESC and present the results in figures 5 and 6 and important figures of merit in table 1. The definitions of various figures of merit are provided in Appendix D.

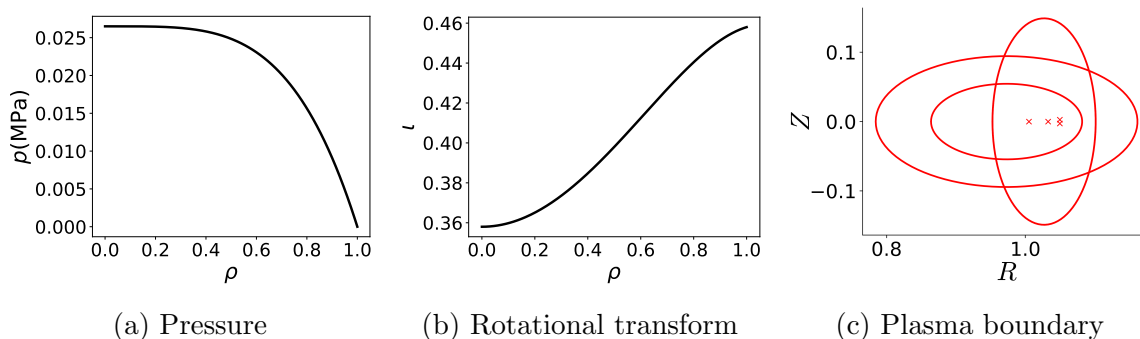


Figure 5: Inputs to the optimization module in DESC for the OP case. Figures (a) and (b) show the various profiles and figure (c) has the boundary cross-section at different toroidal angles for a single field period.

Using DESC, we are able to successfully stabilize the initially unstable equilibrium while maintaining reasonable poloidal omnigenity. Due to the curvature objective, the boundary has a minimal “bean”-like shaping along with a large mirror ratio $(B_{\text{max}} + B_{\text{min}})/(B_{\text{max}} - B_{\text{min}})$, which would simplify coil design. As we stabilize the ideal ballooning mode, we also see a reduction in the maximum KBM growth rate. Moreover, since this equilibrium has a negative shear, we hypothesize that it will have a reduced

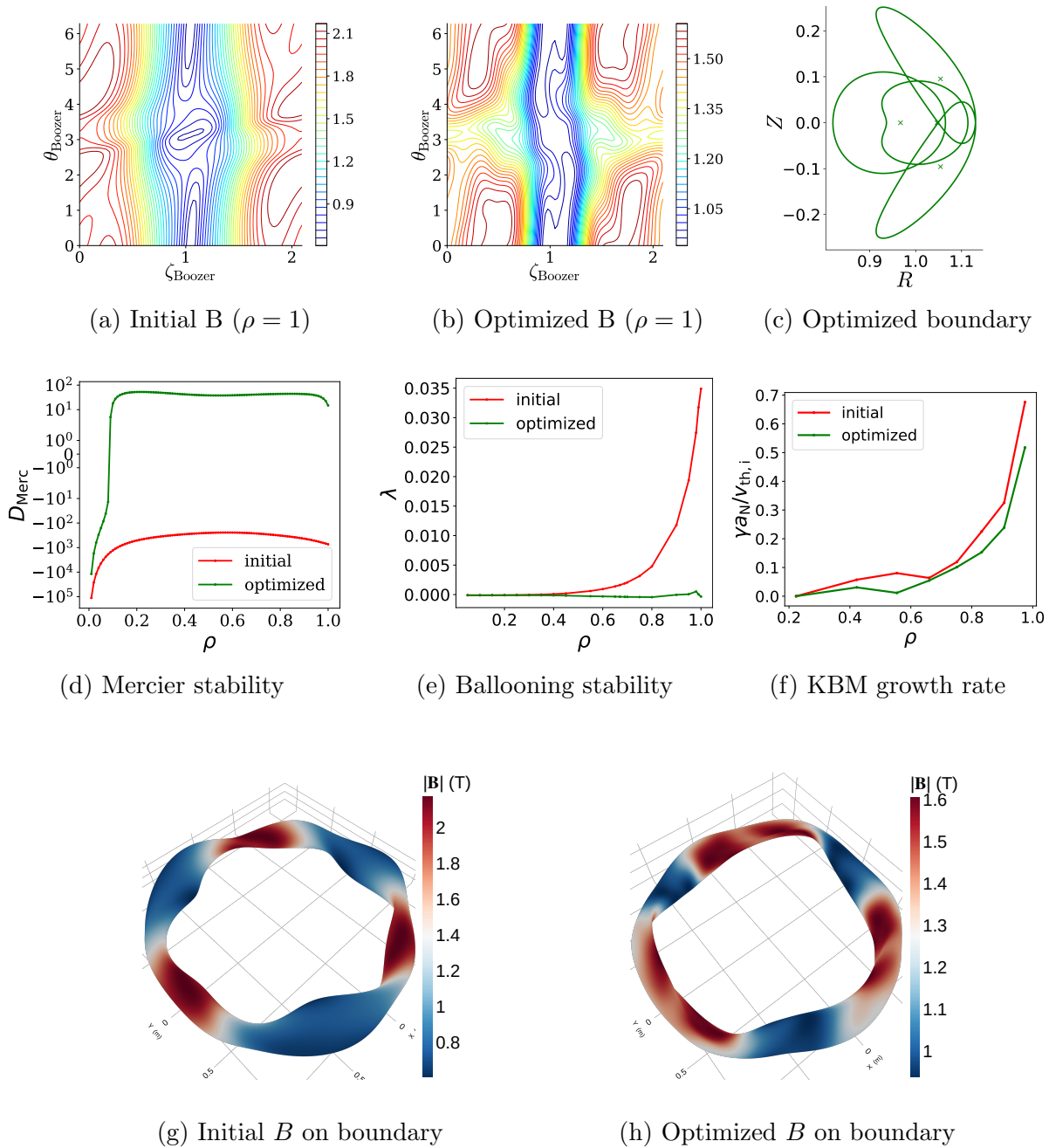


Figure 6: Outputs from the OP stability optimization in DESC. Figures (a) and (b) show the magnetic field strength B on the boundary surface, respectively; (c) is the optimized boundary cross-section at different toroidal angles for a single field period. Figures (d), (e), (f) compare various instabilities between the initial and optimized equilibria and figures (g), (h) illustrate the magnetic field strength on the plasma boundary.

Table 1: Figures of merit of the initial and optimized OP equilibria

Equilibrium	Aspect ratio	$\langle\beta\rangle$	OP error	$\Psi_b(\text{T} - \text{m}^2)$	$I_b(\text{kA})$
initial	9.33	0.032	2.02	0.037	-5.3
optimized	9.82	0.029	0.20	0.037	31.9

turbulent transport compared to that of an equilibrium with a positive shear. Since the rotational transform does not cross any low-order rational values, this equilibrium will not form any low-order magnetic islands. The negative shear will also stabilize any bootstrap-current driven high-order magnetic islands [40].

In the next section, we generate a toroidally omnigenous equilibrium using the same process.

6.2. Toroidal omnigenity (OT)

In this section, we will find a toroidally omnigenous (OT) equilibrium with improved stability using DESC. To obtain toroidal omnigenity, we start with a equilibrium that is ballooning-stable and close to quasisymmetry from the omnigenity database. The OT database is generated by first calculating quasisymmetric equilibria from pyQSC [41] and then optimizing them for toroidal omnigenity using DESC. The initial equilibrium has a finite- β with $n_{\text{FP}} = 1$ and a negative magnetic shear. The input data are presented in figure 7 and important properties of this equilibrium are given in table 2.

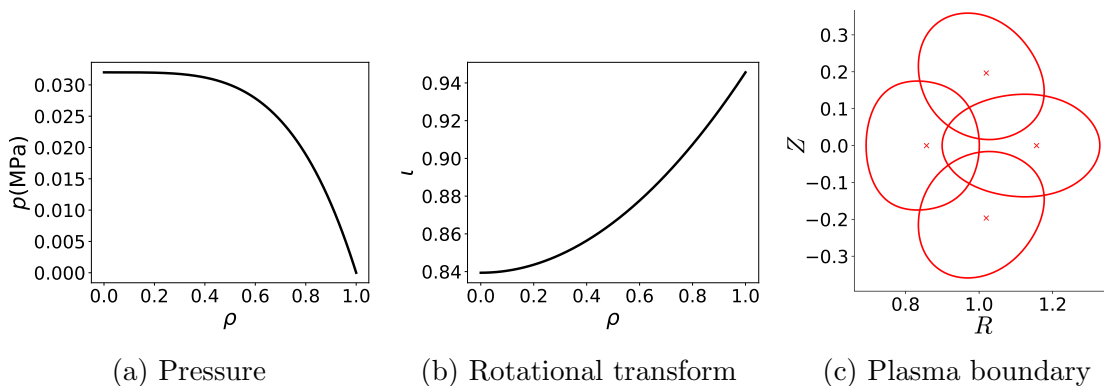


Figure 7: Inputs to the optimization module in DESC. Figures (a) and (b) show the pressure and rotational transform profiles and figure (c) is the initial boundary cross-section at different toroidal angles for a single field period.

We have successfully obtained a toroidal omnigenous equilibrium with improved stability. The equilibrium becomes Mercier stable for most of the volume without degrading the ballooning stability and omnigenity. We also see a small reduction in the KBM growth rate, especially near the plasma edge. Due to the curvature objective, we can again avoid “bean”-like shapes in the inboard side of the optimized stellarator. It is

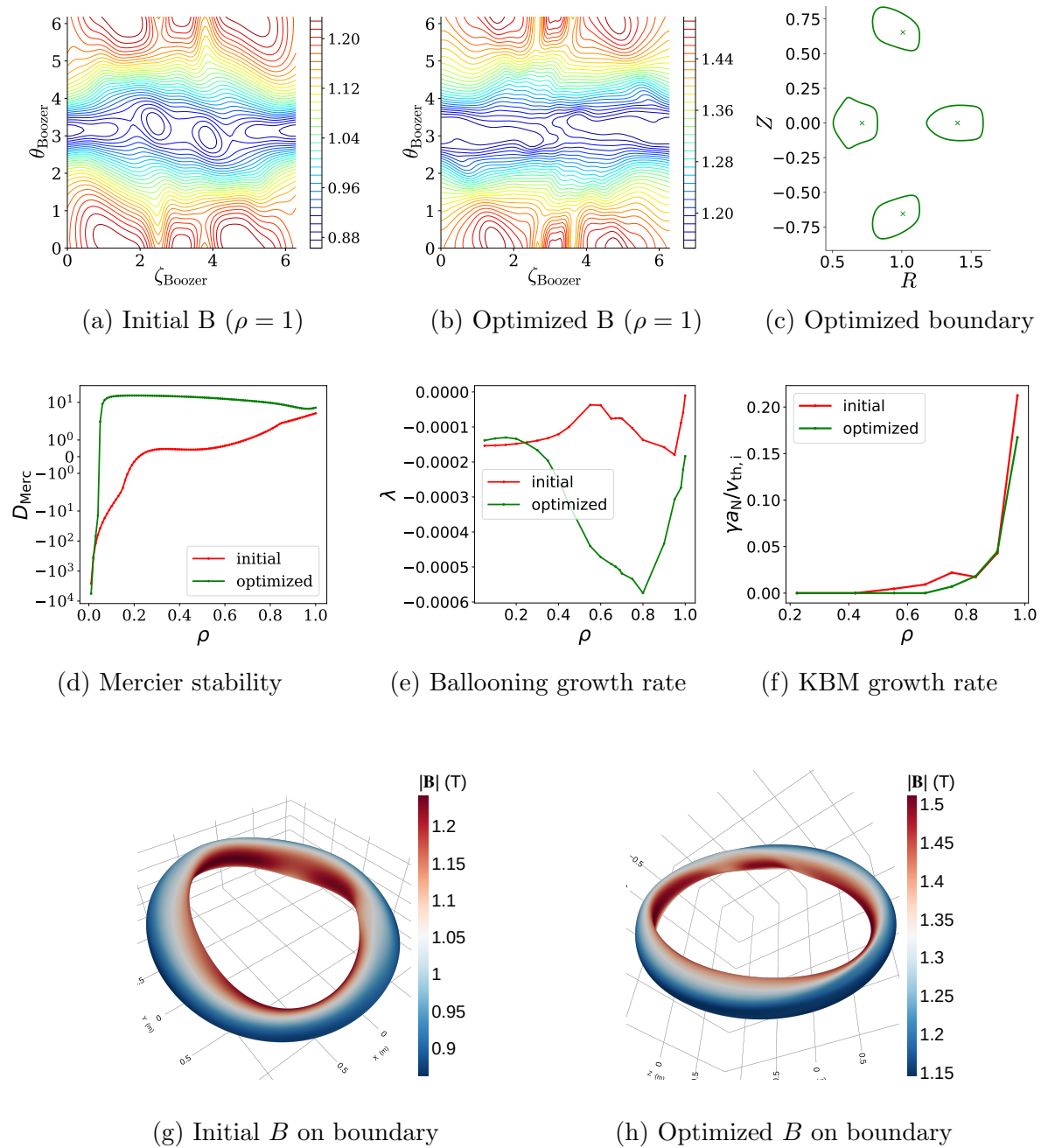


Figure 8: Outputs from the OT stability optimization in DESC. Figures (a) and (b) show the magnetic field strength B on the boundary surface, respectively; (c) is the optimized boundary cross-section at different toroidal angles for a single field period, figures (d), (e), (f) show comparison of various instabilities between the initial and optimized equilibria and figures (g), (h) illustrate the magnetic field strength on the plasma boundary.

Table 2: Figures of merit of the initial and optimized OT equilibria

Equilibrium	Aspect ratio	$\langle\beta\rangle$	OT error	$\Psi_b(\text{T} - \text{m}^2)$	$I_b(\text{kA})$
initial	5.92	0.054	0.22	0.087	156
optimized	6.25	0.033	0.04	0.087	151

important to point out that, much like quasisymmetric equilibria, our results indicate that obtaining low-aspect-ratio OT equilibria is simpler than achieving low-aspect-ratio OP or OH equilibria. Note that, even though the magnetic axis of the optimized configuration appears to have a high torsion from figure 8(c), the 3D figure 8(h) reveals that the stellarator axis remains nearly planar.

6.3. Helical omnigenity (OH)

In this section, we will generate a helically omnigenous (OH) equilibrium with improved stability using DESC. To obtain helical omnigenity, we start with a finite- β circular vacuum equilibrium with $n_{\text{FP}} = 5$ and a finite magnetic axis torsion using the following boundary parametrization

$$R_b = 1 + 0.1 \cos(\theta) + 0.1 \cos(5\phi) \quad (36a)$$

$$Z_b = 0.1 \sin(\theta) + 0.1 \sin(5\phi) \quad (36b)$$

The shape of this equilibrium and input profiles are provided in figure 9 and its characteristic properties are given in table 3. Using DESC, we are able to successfully

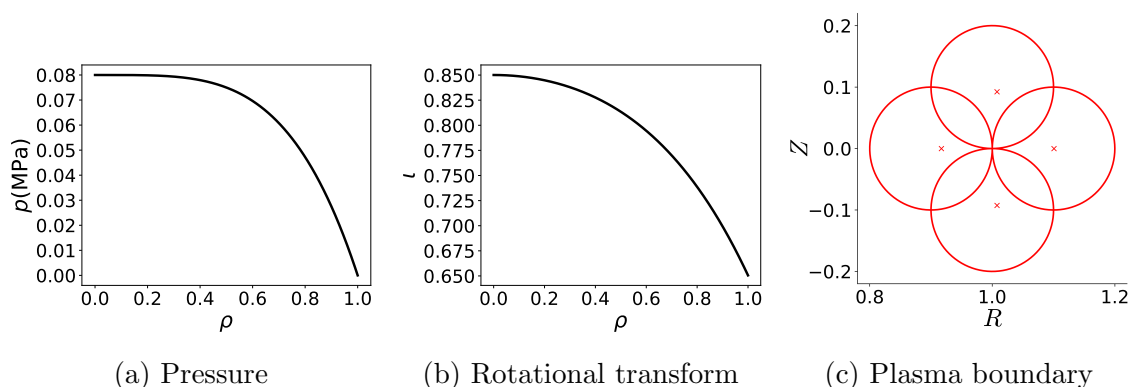


Figure 9: Inputs to the optimization module in DESC for the OH case. Figures (a) and (b) show the pressure and rotational transform profiles and figure (c) is the boundary cross-section at different toroidal angles for a single field period.

stabilize the equilibrium while improving the quality of omnigenity. However, we find that obtaining a stable OH is more difficult compared to the OP or OT for a high plasma beta. The optimized equilibria are also strongly “bean”-shaped which would affect coil

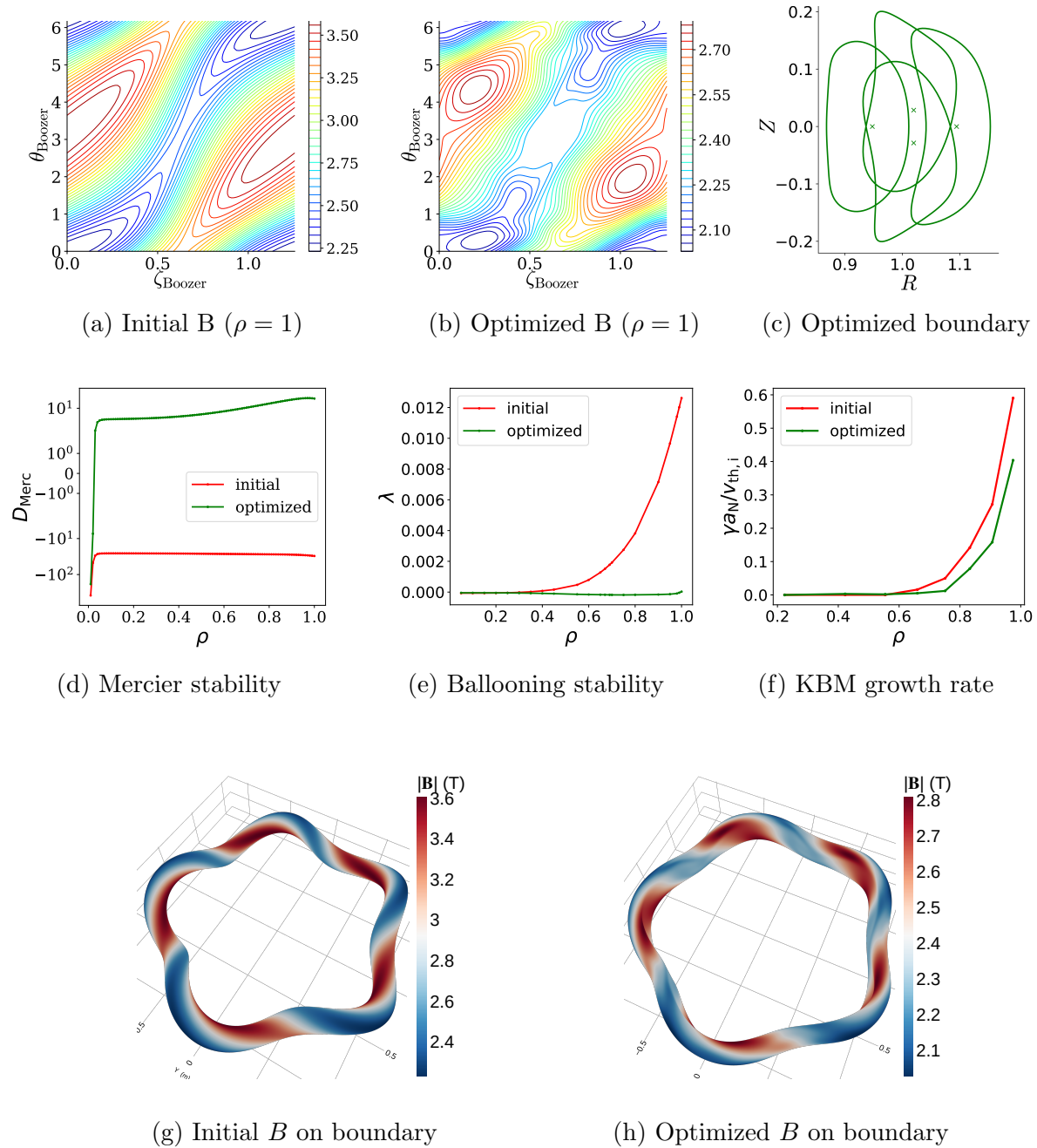


Figure 10: Outputs from the OH stability optimization in DESC. Figures (a) and (b) show the magnetic field strength B on the boundary surface, respectively; (c) is the optimized boundary cross-section at different toroidal angles for a single field period, figures (d), (e), (f) show comparison of various instabilities between the initial and optimized equilibria and figures (g), (h) illustrate the magnetic field strength on the plasma boundary.

Table 3: Figures of merit of the initial and optimized OH equilibria

Equilibrium	Aspect ratio	$\langle\beta\rangle$	OH error	$\Psi_b(\text{T} - \text{m}^2)$	$I_b(\text{kA})$
initial	10.0	0.016	0.32	0.079	23.8
optimized	9.37	0.025	0.21	0.079	120

design. Positive shear would also degrade turbulent transport compared to negative shear equilibria.

The distance from ideal ballooning marginality significantly reduced the KBM growth rate for the OH case, but not for the OP and OT case. This indicates that our hypothesis correlating the distance from marginality and the KBM growth rate is not always correct. To determine the cause of this inconsistency, we perform an additional analysis in the next section.

7. $\hat{s} - \alpha_{\text{MHD}}$ analysis of the optimized omnigenous equilibria

In this section we analyze the ideal MHD and kinetic properties of the three optimized equilibria and determine when the distance from marginality proxy is suitable to reduce the KBM growth rates. To do so, we start by plotting the ideal ballooning growth rates in the $\hat{s} - \alpha_{\text{MHD}}$ landscape for the three optimized equilibria at four different radii. To create a single $\hat{s} - \alpha_{\text{MHD}}$ contour plot, we solve the ballooning equation for $N_{\hat{s}} = 24 \times N_{\alpha_{\text{MHD}}} = 32$. For each solution, we use $\zeta = [-5\pi, 5\pi]$, $N = 1961$ points along a field line and scan $N_{\alpha} = 8$ field lines with $\alpha \in [0, \pi]$ and $N_{\zeta_0} = 9$ values of $\zeta_0 \in [-\pi/2, \pi/2]$.

7.1. Optimized OP equilibrium

The $\hat{s} - \alpha_{\text{MHD}}$ landscape for the OP equilibrium is shown in figure 11. We demonstrate

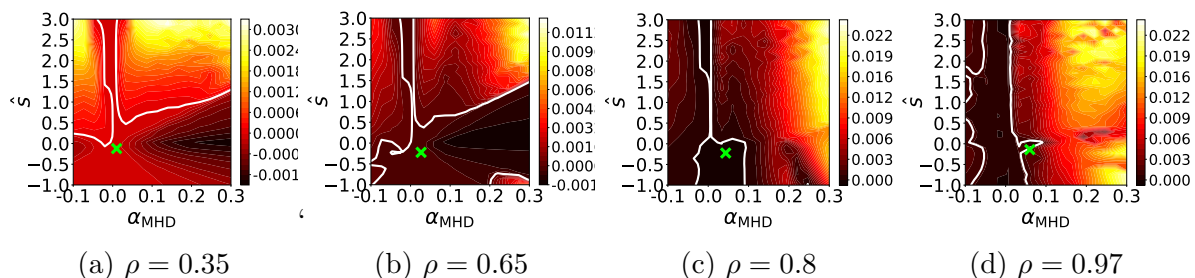


Figure 11: $\hat{s} - \alpha_{\text{MHD}}$ scans of the ideal ballooning growth rate for the optimized OP configuration. The white line corresponds to the marginal stability curve. The nominal equilibrium (marked by a cross) always lies in the first stability region and access to second stability in the outer core, is inaccessible.

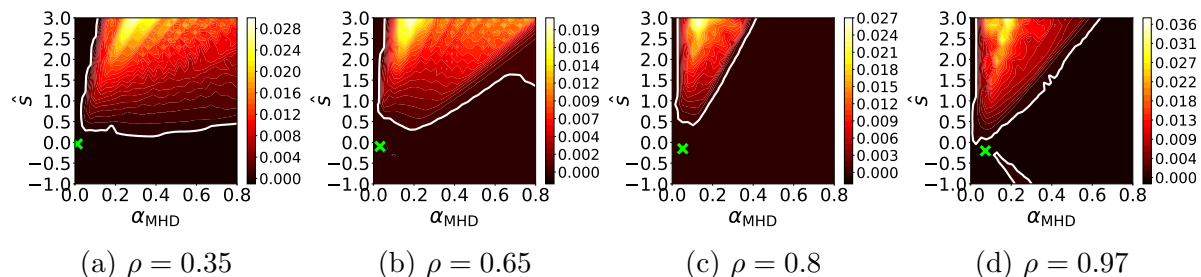


Figure 12: $\hat{s} - \alpha_{\text{MHD}}$ scans of the optimized OT configuration. The nominal equilibrium (marked by a cross) moves from the first to the second stable region as we move from the core to the edge. Second stability is fully accessible

the existence of a second stability regime in the core region in poloidally omnigenous stellarators. However, as we move towards the outer core, second stability becomes inaccessible for this equilibrium. This suggests that despite the existence of this state, it might not be realistically achievable. When pressure rises from a vacuum equilibrium ($\alpha_{\text{MHD}} = 0$) and the equilibrium enters the unstable region KBM will drastically increase heat and particle transport, preventing the pressure profile from becoming steeper. Therefore, one must check accessibility by repeating this exercise, especially for high- β omnigenous stellarators such as the ones developed by Sanchez *et al* [42] and Goodman *et al* [43].

7.2. Optimized OT equilibrium

The $\hat{s} - \alpha_{\text{MHD}}$ landscape for the OP equilibrium is shown in figure 11. Similar to the OP case, we find that the OT equilibrium is situated in the second stability region, demonstrating the existence of a second stability regime in toroidally omnigenous stellarators. Moreover, for these equilibria, second stability is accessible and is not blocked by an unstable region. This means that one can achieve this state without crossing an unstable region — a region of large turbulent transport resulting from unstable ideal and kinetic ballooning modes.

7.3. Optimized OH equilibrium

The $\hat{s} - \alpha_{\text{MHD}}$ landscape for the OH equilibrium is shown in figure 13. Unlike the OP and OT cases, we find that the OH equilibrium is situated in the first stability region. Although a second stability region is present, the outer core equilibria cannot access it. It may be possible to access second stability for negative shear OH equilibria.

7.4. When is the distance from marginality a good proxy for KBMs?

For the OP and OT equilibria, the KBM growth rates did not change significantly even when we stabilized the ideal ballooning mode and increased the distance from marginality, whereas for the OH case, the KBM growth rate decreased significantly.

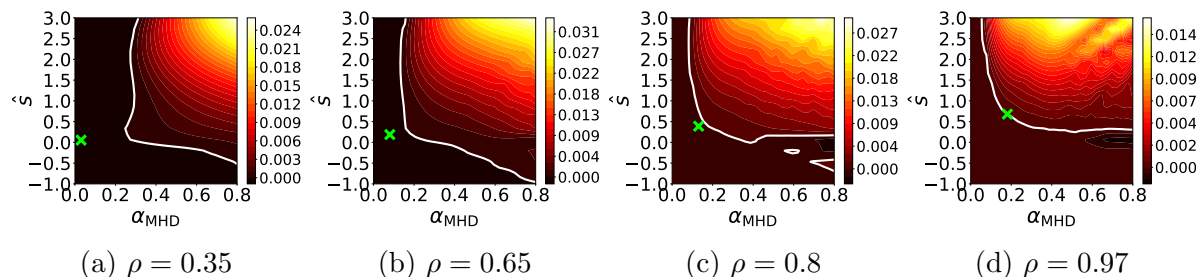


Figure 13: $\hat{s} - \alpha_{\text{MHD}}$ scans of the optimized OH configuration. The nominal equilibrium (marked by a cross) always lies in the first stability region. Second stability seems to exist near the edge but it is inaccessible.

Therefore, we hypothesize that the distance from ballooning marginality proxy is only effective in reducing the KBM growth rate when the equilibrium is ballooning unstable or close to marginal stability.

8. Summary and Conclusions

In this work, we found omnigenous high- β stellarators with enhanced stability — stability against Mercier, ideal ballooning, and kinetic ballooning modes using the fast, GPU-accelerated DESC optimizer. We explained different objectives and presented three stellarator examples with poloidal, toroidal, and helical omnigenity. We found the existence of a region of second stability against the ideal ballooning mode in all three cases. The second stable region was only accessible for the toroidally omnigenous (OT) case. We found that the distance from ideal ballooning marginality is only a good proxy for KBMs if an equilibrium is ballooning unstable or close to marginally stability.

This work presents many avenues for future research. A key step forward would be to extend the stability optimization to ensure low- n MHD stability. This is especially important for the OT and OH cases since they require a significant plasma current. This can be done with the help of new faster codes like DCON3D [44, 45]. We must also evaluate neoclassical transport to ensure that the confinement is not limited by transport due to $1/\nu$ or $\sqrt{\nu}$ regime. To ensure optimization against KBMs, we can also couple DESC with a fully electromagnetic solver such as GS2 and perform direct optimization, as demonstrated in Gaur [46](pp. 110-114) or a linear adjoint gyrokinetic solver, based on the technique demonstrated by Acton [47] *et al*. This will allow us to directly reduce the growth rate of any unstable gyrokinetic mode. To reduce nonlinear heat and particle transport, one could also implement equilibrium-dependent proxies for nonlinear heat fluxes resulting from KBMs using improved quasilinear models.

Since the $\hat{s} - \alpha_{\text{MHD}}$ analysis is valid for any radially local calculation and to ensure that the ion temperature is not limited by electrostatic (low β) turbulence, it is important to apply it to a local gyrokinetic turbulence code and understand the behavior of kinetic turbulence. $\hat{s} - \alpha_{\text{MHD}}$ analysis of nonlinear heat and particle fluxes will be

presented in a subsequent paper.

Data availability The driver and post-processing scripts along with the optimized omnigenous equilibria used in this paper are freely available in this Zenodo repository. The DESC code is open source and can be obtained, along with tutorials for omnigenicity and ballooning stability from this GitHub repository. Similarly, the GS2 code is open source and can be acquired from this repository. In this work, we use an image of the GS2 source, which is freely available here.

Acknowledgements One of the authors, R. G. enjoyed fruitful discussions with W. Sengupta, X. Chu, M. Landreman, F. P. Diaz, I. G. Abel, M. Zarnstroff, M. Hardman, N. Barbour and B. Jang. This work is funded through the SciDAC program by the US Department of Energy, Office of Fusion Energy Science, and Office of Advanced Scientific Computing Research under contract No. DE-AC02-09CH11466, the Hidden Symmetries Grant from the Simons Foundation/SFARI (560651, AB), and Microsoft Azure Cloud Computing mini-grant awarded by the Center for Statistics and Machine Learning (CSML), Princeton University. This research also used the computing resources of the Della, Stellar, and Traverse clusters at Princeton University.

Appendix A. The DESC optimizer suite

DESC [7–10] is an equilibrium solver and optimizer, designed primarily to generate and optimize stellarator equilibria. It solves the ideal MHD force balance equation (3) as an inverse problem — obtaining the cylindrical coordinates (R, ζ, ϕ) by defining a grid in a set of non-orthogonal curvilinear coordinates (ψ, θ, ϕ) . For a fixed boundary system, the user has to specify the pressure $p(\psi)$ and the enclosed toroidal current $I(\psi)$, or the rotational transform $\iota(\psi)$ along with the boundary shape $R_b(\theta, \zeta)$, $Z_b(\theta, \zeta)$, and the enclosed toroidal flux by the boundary ψ_b . Given these inputs, DESC solves (3) to find the magnetic field \mathbf{B} and the shape of the flux surfaces throughout the volume. DESC uses a (ρ, θ, ϕ) coordinate system, where

$$\rho = \sqrt{\frac{\psi}{\psi_b}}, \quad (\text{A.1})$$

$$\theta = \theta_* - \Lambda, \quad (\text{A.2})$$

$$\zeta = \phi, \quad (\text{A.3})$$

The problem is defined in a cylindrical coordinate system (R, ζ, Z) by decomposing it into Fourier-Zernike spectral bases as shown below

$$R(\rho, \theta, \zeta) = \sum_{m=-M, n=-N, l=0}^{M, N, L} R_{lmn} \mathcal{Z}_l^m(\rho, \theta) \mathcal{F}^n(\zeta) \quad (\text{A.4})$$

$$\Lambda(\rho, \theta, \zeta) = \sum_{m=-M, n=-N, l=0}^{M, N, L} \Lambda_{lmn} \mathcal{Z}_l^m(\rho, \theta) \mathcal{F}^n(\zeta) \quad (\text{A.5})$$

$$Z(\rho, \theta, \zeta) = \sum_{m=-M, n=-N, l=0}^{M, N, L} Z_{lmn} \mathcal{Z}_l^m(\rho, \theta) \mathcal{F}^n(\zeta) \quad (\text{A.6})$$

where l, m , and n are the radial, poloidal, and toroidal mode numbers whereas L, M , and N define the largest values of l, m , and n , respectively. This defines the resolution of a DESC equilibrium. The Zernike polynomials $\mathcal{Z}_l^m(\rho, \theta)$ are defined as

$$\mathcal{Z}_l^m(\rho, \theta) = \begin{cases} \mathcal{R}_l^m(\rho) \cos(m\theta) & \text{for } m \geq 0 \text{ and } 0 \leq \rho \leq 1 \\ \mathcal{R}_l^{|m|}(\rho) \sin(|m|\theta) & \text{for } m < 0 \text{ and } 0 \leq \rho \leq 1 \end{cases}, \quad (\text{A.7})$$

where

$$\mathcal{R}_l^m(\rho) = \sum_{s=0}^{(l-m)/2} \frac{(-1)^s (l-s)!}{s! \left(\frac{l+m}{2} - s\right)! \left(\frac{l-m}{2} - s\right)!} \rho^{l-2s} \quad \text{for } m \geq 0, \quad (\text{A.8})$$

denotes the radial variation using shifted Jacobi polynomials.

Using cylindrical coordinates and duality relations between cylindrical and curvilinear coordinates (ψ, θ, ζ) , we can calculate all terms in (3). Additionally, we impose the constraint $\mathbf{B} \cdot \nabla \rho = 0$, enforcing the toroidal nestedness of all flux surfaces.

This reduces the system from three to two coupled partial differential equations in three dimensions

$$F_\rho = \frac{1}{\mu_0} \left[B^\zeta \left(\frac{\partial B_\rho}{\partial \zeta} - \frac{\partial B_\zeta}{\partial \rho} \right) - B^\theta \left(\frac{\partial B_\theta}{\partial \rho} - \frac{\partial B_\rho}{\partial \theta} \right) \right] - \frac{dp}{d\rho}, \quad (\text{A.9})$$

$$F_{\beta_{\text{DESC}}} = \frac{1}{\mu_0} \left(\frac{\partial B_\zeta}{\partial \theta} - \frac{\partial B_\theta}{\partial \zeta} \right), \quad (\text{A.10})$$

where a subscript x denotes the covariant component $F_x = (\mathbf{F} \cdot \mathbf{e}^x)$ and superscript denotes the contravariant component $F^x = (\mathbf{F} \cdot \mathbf{e}_x)$ and the direction vector

$$\beta_{\text{DESC}} = (B^\zeta \mathbf{e}^\theta - B^\theta \mathbf{e}^\zeta). \quad (\text{A.11})$$

Using this formalism, combined with the nestedness assumption, DESC minimizes the two components of the force error \mathbf{F} , which gives us the desired equilibrium.

Using the spectral representation, it becomes possible to accurately express any continuous optimizable quantity as a combination of the components of \mathbf{B} and the input parameters. This capability enables us to optimize multiple objectives simultaneously, rather than solely minimizing the force balance error. In addition, by combining this spectral solver with the GPU-accelerated JAX [48] package, we can efficiently and accurately compute the gradients of any quantity using automatic differentiation. This enables us to perform rapid optimization using gradient-based methods, as demonstrated in the main body of this paper.

Appendix B. Local variation of a 3D equilibrium

In this section, we will briefly explain the method of local variation of gradients, first developed by Greene and Chance [17] for tokamaks and later by Hegna and Nakajima [18] for stellarators. Using this method, one can vary the gradients $p'(\psi)$ and $i'(\psi)$ on a flux surface while locally satisfying the ideal MHD force balance. By varying these gradients, and consequently the local equilibrium around a flux surface, we can obtain a deeper understanding of the characteristics of tokamaks and stellarators in relation to small-scale instabilities. We use this analysis to vary the normalized pressure gradient α_{MHD} , and global shear \hat{s} and to calculate the growth rates against the ideal ballooning and the kinetic ballooning instabilities.

We start by writing the magnetic field in Boozer coordinates

$$\mathbf{B} = \nabla\psi \times \nabla(\theta_{\text{B}} - \iota\zeta_{\text{B}}) \quad (\text{B.1})$$

and equivalently defined as

$$\mathbf{B} = G(\psi) \nabla\zeta_{\text{B}} + I(\psi) \nabla\theta_{\text{B}} + \hat{\beta} \nabla\psi, \quad (\text{B.2})$$

where $G(\psi)$ is the enclosed poloidal current, $I(\psi)$ is the enclosed toroidal current and $\hat{\beta}$ is related to the Pfirsch-Schlüter current. We also define the Jacobian

$$\sqrt{g_{\text{B}}} = [(\nabla\psi \times \nabla\theta_{\text{B}}) \cdot \nabla\zeta_{\text{B}}]^{-1} = \frac{G + \iota I}{B^2} \quad (\text{B.3})$$

To ensure both the definitions (B.1) and (B.2) of the magnetic field are consistent, we must ensure

$$G = \frac{g_{\zeta_B \zeta_B} + \iota g_{\zeta_B \theta_B}}{\sqrt{g_B}} \quad (\text{B.4})$$

$$I = \frac{g_{\zeta_B \theta_B} + \iota g_{\theta_B \theta_B}}{\sqrt{g_B}} \quad (\text{B.5})$$

$$\hat{\beta} = \frac{g_{\zeta_B \psi} + \iota g_{\theta_B \psi}}{\sqrt{g_B}} \quad (\text{B.6})$$

where g_{ab} is the metric tensor element $(\partial \mathbf{x} / \partial a) \cdot (\partial \mathbf{x} / \partial b)$. Substituting (B.2) into (3), and separating the radial component, we get

$$-G' - \iota I' + \left(\frac{\partial}{\partial \zeta_B} + \iota \frac{\partial}{\partial \theta_B} \right) \hat{\beta} = p' \sqrt{g_B}. \quad (\text{B.7})$$

Applying the surface averaging operator $\oint = (1/2\pi)^2 \int d\theta_B \int d\zeta_B$ to (B.7), we get the surface-averaged force balance equation

$$-G' - \iota I' = p' V'. \quad (\text{B.8})$$

Subtracting (B.8) from (B.7), we get an equation for the variable $\hat{\beta}$

$$\left(\frac{\partial}{\partial \zeta_B} + \iota \frac{\partial}{\partial \theta_B} \right) \hat{\beta} = p' (\sqrt{g_B} - V'). \quad (\text{B.9})$$

Variables such as G' , I' , and $\hat{\beta}$ will change when we locally vary the pressure gradient to maintain force balance. A final quantity of interest is the Pfirsch-Schlüter current

$$\lambda = \frac{1}{p' V'} \left(\frac{\mathbf{J} \cdot \mathbf{B}}{B^2} - \oint \frac{\mathbf{J} \cdot \mathbf{B}}{B^2} \right) = (\mathbf{B} \times \nabla \psi) \cdot \nabla \hat{\beta}. \quad (\text{B.10})$$

With all the important expressions, we proceed to demonstrate the method of variation of a local equilibrium. We expand all flux functions in a local coordinate $y = (\psi - \psi_0)/\mu$ about the flux surface labelled ψ_0

$$p = p^{(0)}(\psi) + \mu p^{(1)}(y) + \mu^2 p^{(2)}(y) + \dots, \quad (\text{B.11})$$

$$\iota = \iota^{(0)}(\psi) + \mu \iota^{(1)}(y) + \mu^2 \iota^{(2)}(y) + \dots, \quad (\text{B.12})$$

$$G = G^{(0)}(\psi) + \mu G^{(1)}(y) + \mu^2 G^{(2)}(y) + \dots, \quad (\text{B.13})$$

$$I = I^{(0)}(\psi) + \mu I^{(1)}(y) + \mu^2 I^{(2)}(y) + \dots, \quad (\text{B.14})$$

where $\mu \ll 1$. This expansion allows us to vary the gradients of the flux functions by the same order as $p(\psi_0)$ while varying the equilibrium values by order μ . This also changes the position of a points \mathbf{x} on a flux surface

$$\mathbf{x} = \mathbf{x}^{(0)}(\psi, \theta_B, \zeta_B) + \mu \mathbf{x}^{(1)}(y, \theta_B, \zeta_B) + \dots \quad (\text{B.15})$$

and the variable

$$\hat{\beta} = \hat{\beta}^{(0)}(\psi, \theta_B, \zeta_B) + \mu \hat{\beta}^{(1)}(y, \theta_B, \zeta_B) + \dots \quad (\text{B.16})$$

Varying the local gradient would require calculating the gradient of the quantities in the series expansion — the only gradients that will be comparable to the lowest-order

gradients will be in terms of the form $\partial/\partial y$. Therefore, solving for these gradients will fully define the new equilibrium.

First, we substitute (B.16) and into (B.9) to get

$$\left(\frac{\partial}{\partial \zeta_B} + \iota \frac{\partial}{\partial \theta_B}\right) \hat{\beta}^{(1)} = p^{(1)'} (\sqrt{g_B} - V'). \quad (\text{B.17})$$

Since we know $\partial \mathbf{x} / \partial y$ is a general three-dimensional vector

$$\frac{\partial \mathbf{x}}{\partial y} = C \mathbf{B} + D \frac{\mathbf{B} \times \nabla \psi}{B^2} + M \frac{\nabla \psi}{|\nabla \psi|^2} \quad (\text{B.18})$$

Next, using (B.2), (B.16), and (B.6) gives us $C = \hat{\beta}^{(1)}/B^2$. Similarly, enforcing that the jacobian $\sqrt{g_B}$ remains fixed after varying the pressure, we get $M = 0$. The final and most important quantity in this analysis, the cross-field variation D , can be obtained by substituting (B.18) into constraints (B.4)-(B.5). After some algebraic manipulations, using (B.9) and the flux surface averaging operator, we obtain

$$\left(\frac{\partial}{\partial \zeta_B} + \iota \frac{\partial}{\partial \theta_B}\right) D = \iota^{(1)'} \frac{1}{\oint 1/g^{\psi\psi}} \left(\frac{1}{g^{\psi\psi}} - \oint \frac{1}{g^{\psi\psi}}\right) \quad (\text{B.19})$$

$$- p^{(1)'} \frac{V'(G + \iota I)}{\oint 1/g^{\psi\psi}} \left(\frac{\lambda}{g^{\psi\psi}} \oint \frac{1}{g^{\psi\psi}} - \frac{1}{g^{\psi\psi}} \oint \frac{\lambda}{g^{\psi\psi}}\right), \quad (\text{B.20})$$

where $g^{\psi\psi} = |\nabla \psi|^2$, and λ is the Pfirsch-Schlüter current, obtained from (B.10). Given the variation in the pressure gradient $p^{(1)'}$ and the rotational transform gradient $\iota^{(1)'}$, this completely defines the new local equilibrium. Once the local equilibrium is defined, we calculate the geometric quantities required to solve (22) and (14)-(17) and understand how they would behave if the pressure gradient or magnetic shear were varied. Hudson and Hegna [49], and Hegna and Nakajima [18] have used this technique to analyze the Mercier and ideal ballooning marginal stability of stellarators. We use the same technique to calculate the ideal ballooning eigenvalues and gyrokinetic growth rates.

In practice, we calculate the coefficients $\hat{\beta}$, λ , $\sqrt{g_B}$ on each flux surface by evaluating the Fourier-Zernike coefficients at a fixed ρ . This gives us the Boozer Jacobian $\sqrt{g_B}$ and its Fourier components, from which we can calculate $\hat{\beta}$ and then λ in Fourier space. Upon conversion of λ to real space, we perform flux surface averaging to calculate the cross-field term D . This gives us all the necessary terms needed to calculate the new set of geometry coefficients for the varied equilibrium.

Appendix C. Simplified linear gyrokinetic model in the intermediate frequency range

In this Appendix, we simplify the linearized gyrokinetic model and show how, subject to a set of assumptions, reduces to the ideal ballooning equation. We start by assuming that the frequency of interest ω is faster than the ion transit frequency, but slower than the electron transit frequency

$$\frac{v_{\text{th},i}}{a_N} \ll \epsilon \omega \ll \epsilon^2 \frac{v_{\text{th},e}}{a_N}, \quad \epsilon \equiv \sqrt{\frac{m_e}{m_i}} \ll 1, \quad (\text{C.1})$$

where $v_{\text{th},i} = \sqrt{2T_i/m_i}$, $v_{\text{th},e} = \sqrt{2T_e/m_e}$ are the thermal speeds of the ions and electrons, respectively. This separation in time scales is a consequence of the difference in the masses of ions and electrons.

In this limit, we can simplify the electron gyrokinetic equation

$$\begin{aligned} i(\omega - \omega_{Ds}) h_e + (\mathbf{b} \cdot \nabla \zeta) w_{\parallel} \frac{\partial h_e}{\partial \zeta} \\ = (\omega - \omega_{*,e}^T) \left[J_0 \left(\frac{k_{\perp} w_{\perp}}{\Omega_e} \right) \left(\varphi - \frac{w_{\parallel} \delta A_{\parallel}}{c} \right) + J_1 \left(\frac{k_{\perp} w_{\perp}}{\Omega_e} \right) \frac{w_{\perp}}{k_{\perp}} \frac{\delta B_{\parallel}}{c} \right] F_{0e} \end{aligned} \quad (\text{C.2})$$

to lowest order as

$$w_{\parallel} (\mathbf{b} \cdot \nabla \zeta) \frac{\partial h_e}{\partial \zeta} = w_{\parallel} (\omega - \omega_{*,e}^T) F_{0s} \frac{\delta A_{\parallel}}{c}, \quad (\text{C.3})$$

which can be integrated to give us

$$h_e^{(p)}(\zeta, E, \hat{\lambda}; \sigma) = \left(1 - \frac{\omega_{*,e}^T}{\omega} \right) \delta \hat{A}_{\parallel} F_{0e} + c_0(\hat{\lambda}), \quad (\text{C.4})$$

where $c_0(\hat{\lambda})$ is a constant of integration and we have defined the line-integrated vector potential

$$\delta \hat{A}_{\parallel}(\zeta; \sigma) = \frac{i\omega}{c} \int_{-\sigma\infty}^{\zeta} \frac{d\zeta}{\mathbf{b} \cdot \nabla \zeta} \delta A_{\parallel}, \quad (\text{C.5})$$

where $\sigma = v_{\parallel}/|v_{\parallel}|$ can either be +1 or -1 depending on the streaming direction of the particle with respect to the background magnetic field. Since all the variables that govern the passing species ($\hat{\lambda} \leq 1/B_{\text{max}}$) satisfy the boundary condition $\lim_{\zeta \rightarrow \pm\infty} \delta \hat{A}_{\parallel} = \lim_{\zeta \rightarrow \pm\infty} h_e = 0$, $c_0(\hat{\lambda}) = 0 \forall \hat{\lambda} \leq 1/B_{\text{max}}$. For trapped particles, we must further solve (C.2) to find $c_0(\hat{\lambda}) \neq 0$.

To calculate the trapped electron response to the fields, we rewrite (C.2) after multiplying both sides with an integrating factor $\exp[-i \int d\theta (\omega - \omega_{Ds}) / (w_{\parallel} \mathbf{b} \cdot \nabla \theta)]$

$$\begin{aligned} w_{\parallel} (\mathbf{b} \cdot \nabla \zeta) \frac{\partial}{\partial \zeta} \left\{ \left[h_e - \left(1 - \frac{\omega_{*,e}^T}{\omega} \right) F_{0e} \delta \hat{A}_{\parallel} \right] e^{-i \int d\zeta (\omega - \omega_{De}) / (w_{\parallel} \mathbf{b} \cdot \nabla \zeta)} \right\} e^{i \int d\zeta (\omega - \omega_{De}) / (w_{\parallel} \mathbf{b} \cdot \nabla \zeta)} \\ = (\omega - \omega_{*,e}^T) \left[\varphi - \left(1 - \frac{\omega_{De}}{\omega} \right) \delta \hat{A}_{\parallel} + \frac{w_{\perp}^2}{\Omega_s} \frac{\delta B_{\parallel}}{c} \right] F_{0s}, \end{aligned} \quad (\text{C.6})$$

and apply the bounce-averaging operation

$$\langle X \rangle = \oint \frac{d\zeta}{(\mathbf{b} \cdot \nabla \zeta)} \frac{X}{|w_{\parallel}|} \Big/ \oint \frac{d\zeta}{(\mathbf{b} \cdot \nabla \zeta)} \frac{1}{|w_{\parallel}|}, \quad (\text{C.7})$$

to (C.6), use integration by parts, and then use (C.4), to find $c_0(\lambda)$ for trapped electrons. This gives us the complete trapped electron response

$$h_{k_{\perp},e}^{(t)} = \left(1 - \frac{\omega_{*,e}^T}{\omega} \right) F_{0e} \delta \hat{A}_{\parallel} + \frac{(\omega - \omega_{*,e}^T)}{(\omega - \langle \omega_{Ds} \rangle)} \left\langle \left[\varphi_{k_{\perp}} - \left(1 - \frac{\omega_{De}}{\omega} \right) \delta \hat{A}_{\parallel} + \frac{w_{\perp}^2}{2\Omega_e} \frac{\delta B_{\parallel}}{c} \right] F_{0s} \right\rangle. \quad (\text{C.8})$$

Note that, to lowest order we have used $J_0(k_{\perp} w_{\perp} / \Omega_e) = 1$, $J_1(k_{\perp} w_{\perp} / \Omega_e) = k_{\perp} w_{\perp} / (2\Omega_e)$ due to the intermediate frequency ordering in (C.1). The total electron response is the sum of the trapped ($1/B_{\text{max}} < \hat{\lambda} \leq 1/B_{\text{min}}$) and passing ($\hat{\lambda} \leq 1/B_{\text{max}}$) distributions.

Next, we repeat the same process for ions. However, the trapped and passing frequency of ions is slower than the frequency of interest ω , so the ion gyrokinetic equation to lowest order becomes

$$h_{k_\perp, i}^{(0)} = \frac{(\omega - \omega_{*,i}^T)}{(\omega - \omega_{Di})} \left[J_0 \left(\frac{k_\perp w_\perp}{\Omega_i} \right) \varphi_{k_\perp} + J_1 \left(\frac{k_\perp w_\perp}{\Omega_i} \right) \frac{w_\perp}{k_\perp} \frac{\delta B_\parallel}{c} \right] F_{0i}, \quad (\text{C.9})$$

Using the expressions for the distribution functions h , we can now calculate their moments and plug those moments into the Maxwell's equations. We calculate the velocity integral in $(E, \hat{\lambda}, \vartheta)$ space

$$\int d^3 \mathbf{w} = 2\pi \sum_\sigma \int dE \sqrt{E} \int \frac{d\hat{\lambda} B}{\sqrt{1 - \hat{\lambda} B}}, \quad (\text{C.10})$$

where $\sum_\sigma h(\sigma) = [h(\sigma = 1) + h(\sigma = -1)]$ takes into account both streaming directions of particles. We now have all the information to write the Maxwell's equations. Substituting the gyrokinetic distribution functions into the quasineutrality equation (15), we obtain

$$(2 - Q)\varphi + Q' \delta \tilde{B}_\parallel + \int_{\text{Tr}} d^3 \mathbf{w} \left(\frac{\omega - \omega_{*,e}^T}{\omega - \langle \omega_{D,e} \rangle} \right) \langle X_e \rangle = \left(1 - \frac{\omega_{*,e}}{\omega} \right) \hat{\psi}, \quad (\text{C.11})$$

where $\hat{\psi} = \sum_\sigma \delta \hat{A} = [\delta \hat{A}(\sigma = 1) + \delta \hat{A}(\sigma = -1)]$ and \int_{Tr} implies integration in $\hat{\lambda}$ for trapped particles only, *i.e.*, over a truncated domain $1/B_{\min} \leq \hat{\lambda} \leq 1/B_{\min}$

$$X_s = \varphi - \left(1 - \frac{\omega_{Ds}}{\omega} \right) \hat{\psi} + J_{1s} \frac{w_\perp}{k_\perp} \frac{\delta B}{c}, \quad (\text{C.12})$$

$$Q = \int d^3 \mathbf{v} \left(\frac{\omega - \omega_{*,i}^T}{\omega - \omega_{Di}} \right) J_0^2 F_{0i}, \quad (\text{C.13})$$

$$Q' = \int d^3 \mathbf{v} \left(\frac{\omega - \omega_{*,i}^T}{\omega - \omega_{Di}} \right) \frac{dJ_0^2}{db} F_{0i}, \quad b = \frac{(k_\perp \rho_i)^2}{2}, \quad (\text{C.14})$$

and a typo has been corrected from equation (3.31) in Tang *et al* to get (C.11). Next, we write Ampere's law governing parallel fluctuations of the magnetic field strength

$$\begin{aligned} \delta \tilde{B}_\parallel = & \frac{4\pi n_0 T_i}{B^2} \left\{ Q' \varphi - R \delta \tilde{B}_\parallel + \left[1 - \frac{\omega_{e,*}}{\omega} (1 + \eta_e) \right] \hat{\psi}_\parallel \right. \\ & \left. + \frac{1}{n_0} \int_{\text{Tr}} d^3 \mathbf{v} F_{e0} \left(\frac{\omega - \omega_{*,e}^T}{\omega - \langle \omega_{D,e} \rangle} \right) \langle X_e \rangle v_\perp^2 \right\}, \end{aligned} \quad (\text{C.15})$$

where

$$R = \int d^3 \mathbf{v} \left(\frac{\omega - \omega_{*,i}^T}{\omega - \omega_{Di}} \right) v_\perp^2 J_1^2 F_{0i}. \quad (\text{C.16})$$

Note that the power of v_\perp has been corrected in (C.16) from Tang *et al*. The final equation comes from substituting the simplified gyrokinetic distribution function in the

equation governing the parallel current j_{\parallel} from Tang *et al*

$$\begin{aligned} \mathbf{b} \cdot \nabla \zeta \frac{\partial}{\partial \zeta} \left[\frac{k_{\perp}^2}{B^2} \mathbf{b} \cdot \nabla \zeta \frac{\partial \hat{\psi}_{\parallel}}{\partial \zeta} \right] = \omega^2 \left\{ \left[Q - \left(1 - \frac{\omega_{*e}}{\omega} \right) \right] \varphi - \left[1 - \frac{\omega_{*e}}{\omega} (1 + \eta_e) \right] \left(\frac{\omega_{\kappa} + \omega_B}{\omega} \right) \hat{\psi} \right\} \\ + \int_{\text{Tr}} d^3 \mathbf{w} \left[\frac{F_{0s}}{n_0} \frac{\omega_{\text{De}}}{\omega} \left(\frac{\omega - \omega_*^T}{\omega - \langle \omega_{\text{De}} \rangle} \right) \langle X_e \rangle \right] \end{aligned} \quad (\text{C.17})$$

where we have corrected an omission and a sign error from Tang *et al* on the right side of (C.17). The model now comprises three coupled integro-differential equations (C.11), (C.15), and (C.17).

It is possible to solve the intermediate-frequency electromagnetic gyrokinetic model numerically as an eigenvalue problem. However, this is beyond the scope of this paper and in this work we shall make a set of additional assumptions and impose subsidiary orderings similar to the ones used by Aleynikova *et al* [50,51] to remove trapped particle effects, assume steep density and temperature gradients, high- β , and long-wavelength modes to reduce the model further. Applying the following orderings

$$k_{\perp} \rho_i \sim \delta^{1/2}, A \sim \delta^2, \beta \sim \delta, \omega_d / \omega \sim \delta, a_N / L_n \sim a_N / L_n \sim 1 / \delta, \delta \gg \epsilon \quad (\text{C.18})$$

we can drop all the trapped particle integrals because the integral over pitch angle has the factor $1 / \sqrt{1 - \lambda B} \sim \sqrt{A} \sim \delta$. This ordering reduces the three coupled differential equations to

$$\varphi = \hat{\psi} \quad (\text{C.19})$$

$$\delta B_{\parallel} = \frac{\beta_i}{2} \hat{\psi}_{\parallel} \quad (\text{C.20})$$

$$(\mathbf{b} \cdot \nabla \zeta) \frac{\partial}{\partial \zeta} \frac{(k_{\perp} \rho_i)^2}{2} (\mathbf{b} \cdot \nabla \zeta) \frac{\partial \hat{\psi}}{\partial \zeta} = \frac{\omega}{\omega_A^2} K \hat{\psi}_{\parallel} \quad (\text{C.21})$$

where

$$\begin{aligned} K = \left\{ \left[Q - \left(1 - \frac{\omega_{*e}}{\omega} \right) \right] \left[\alpha_{0e} \left(1 + \frac{\beta_i}{2} R \right) - \alpha_{1e} \tau Q' \frac{\beta_i}{2} \right] \right. \\ \left. - \frac{\beta_i}{2} (Q' + \alpha_{1e}) \left[\alpha_{0e} Q' + \alpha_{1e} (2 - \tau_e Q) \right] \right\} \\ \left[(2 - \tau_e Q) \left(1 + \frac{\beta_i}{2} R \right) + Q'^2 \frac{\beta_i}{2} \right]^{-1} - \alpha_{1e} \frac{\omega_{\kappa} + \omega_B}{\omega} \end{aligned} \quad (\text{C.22})$$

$\alpha_{ls} = (1 - \frac{\omega_{*s}}{\omega} (1 + l\eta_s))$, $\omega_{*s} = \frac{k_y \rho_s}{2} \frac{w_{\text{th},s}}{L_{n,s}} B$, $\beta_i = 8\pi p_i / B^2$. This effectively requires solving a single ODE. We simplify Q, Q' ,

$$\begin{aligned} Q = \left(1 - \frac{\omega_{*,j}}{\omega} \right) + \left(\frac{\omega_B + \omega_{\kappa}}{\omega} - \frac{(k_{\perp} \rho_i)^2}{2} \right) \left(1 - \frac{\omega_{*}}{\omega} (1 + \eta_{i,j}) \right) + \mathcal{O}(\delta^2) \\ Q' = - \left[\left(1 - \frac{\omega_{*,j}}{\omega} (1 + \eta) \right) \right] - \left[\frac{2\omega_B + \omega_{\kappa}}{\omega} + \frac{3}{4} \frac{(k_{\perp} \rho_i)^2}{2} \right] \left[\left(1 - \frac{\omega_{*,j}}{\omega} (1 + 2\eta) \right) \right] + \mathcal{O}(\delta^2) \end{aligned} \quad (\text{C.23})$$

substitute into (C.23) and simplify

$$K = -2 \frac{\omega_{*,i}}{\omega} (1 + \eta) \omega_{\kappa} \hat{\psi}_{\parallel} + \frac{\omega^2}{\omega_A^2} b \hat{\psi}_{\parallel}. \quad (\text{C.24})$$

Finally, substituting K in , we recover the infinite- n ideal ballooning equation

$$\mathbf{b} \cdot \nabla \zeta \frac{\partial}{\partial \zeta} b(\mathbf{b} \cdot \nabla \zeta) \frac{\partial \hat{\psi}_{\parallel}}{\partial \zeta} + 2 \frac{dp}{d\psi} (k_y \rho_r) \omega_{\kappa} \hat{\psi}_{\parallel} = \frac{\omega^2}{\omega_A^2} b \hat{\psi}_{\parallel} \quad (\text{C.25})$$

Details such as identities and algebra used to obtain these equations are presented in the supplementary notes.

Appendix D. Definition of various objectives and figures of merit used in DESC

In this appendix, we will explain the definition of various objective functions and figures of merit used by us in the main body of this paper.

Appendix D.1. Objective functions

We start by defining the curvature objective

$$f_{\text{curv}} = \text{ReLU}(\max(\kappa_{2,\rho} - \kappa_{2,\rho,\text{bound1}}, \kappa_{2,\rho} - \kappa_{2,\rho,\text{bound2}})) \quad (\text{D.1})$$

where

$$\kappa_{2,\rho} = \min \left\{ x : \det \begin{bmatrix} L_{\text{sff},\rho} - xE & M_{\text{sff},\rho} - xF \\ M_{\text{sff},\rho} - xF & N_{\text{sff},\rho} - xG \end{bmatrix} = 0 \right\}$$

is the second principal curvature on a given point on a flux surface, and

$$E = \frac{\partial \mathbf{x}}{\partial \zeta} \cdot \frac{\partial \mathbf{x}}{\partial \zeta}, \quad F = \frac{\partial \mathbf{x}}{\partial \rho} \cdot \frac{\partial \mathbf{x}}{\partial \zeta}, \quad G = \frac{\partial \mathbf{x}}{\partial \rho} \cdot \frac{\partial \mathbf{x}}{\partial \rho}, \quad (\text{D.2})$$

$$L_{\text{sff},\rho} = \frac{\partial^2 \mathbf{x}}{\partial \theta^2} \cdot \frac{\nabla \rho}{|\nabla \rho|}, \quad M_{\text{sff},\rho} = \frac{\partial^2 \mathbf{x}}{\partial \theta \partial \zeta} \cdot \frac{\nabla \rho}{|\nabla \rho|}, \quad N_{\text{sff},\rho} = \frac{\partial^2 \mathbf{x}}{\partial \zeta^2} \cdot \frac{\nabla \rho}{|\nabla \rho|} \quad (\text{D.3})$$

are the metric coefficients corresponding to the first and second fundamental forms. The user-specified values $\kappa_{2,\text{bound1}}, \kappa_{2,\text{bound2}}$ define the limits on the curvature. Using this objective, we impose a maximum and minimum value on $\kappa_{2,\rho}$ that helps the optimizer avoid plasma boundaries with sharp convex or concave curvatures.

To maintain a shape that is practically feasible using coils, we also put bounds on the elongation of the boundary, by using the elongation objective

$$f_{\text{elongation}} = \text{ReLU}(\max e - e_{\text{bound1}}, e - e_{\text{bound2}}) \quad (\text{D.4})$$

where

$$e = \frac{1}{2\pi} \int \hat{e} d\zeta, \quad \hat{e} = \frac{a_{\text{major}}}{a_{\text{minor}}} \quad (\text{D.5})$$

is the averaged elongation of a flux surface averaged over the cylindrical toroidal angle ζ , \hat{e} is the elongation of a toroidal cross-section, and e_{bound} are the bounds imposed on the elongation. To calculate \hat{e} , we first calculate a_{major} using the area \hat{A} and perimeter

\hat{P} of a toroidal cross-section and invert Ramanujan's approximation for the perimeter of an ellipse [52, 53]

$$a_{\text{major}} = \frac{\sqrt{3} \left(\sqrt{8\pi\hat{A} + \hat{P}^2} + \sqrt{\left| 2\sqrt{3}\hat{P}\sqrt{8\pi\hat{A} + \hat{P}^2} - 40\pi\hat{A} + 4\hat{P}^2 \right|} \right) + 3\hat{P}}{12\pi} \quad (\text{D.6})$$

Using the major radius a_{major} , the area \hat{A} , and assuming the section has an elliptical shape, we get $a_{\text{minor}} = \hat{A}/(\pi a_{\text{major}})$ which gives us the elongation $\hat{e} = a_{\text{major}}/a_{\text{minor}}$ and the average elongation e .

Finally, we define the Mercier (or interchange) stability objective

$$f_{D_{\text{Merc}}} = (D_{\text{Merc}} - D_{\text{Merc}0}), \quad (\text{D.7})$$

where

$$D_{\text{Merc}} = -\frac{p'}{l'} V^{\dagger\dagger} - \frac{1}{4} > 0, \quad (\text{D.8})$$

where the quantity $V^{\dagger\dagger}$ is related to the magnetic well [54]. A $D_{\text{Merc}} > 0$ corresponds to stability against interchange modes, whereas $D_{\text{Merc}} < 0$ implies ideal interchange instability. Note that for negative shear equilibria, $D_{\text{Merc}} > 0$ implies a positive (favorable) magnetic well $V^{\dagger\dagger} > 0$, which is the case for OP and OT cases presented in this paper.

Appendix D.2. Figures of Merit

In this section, we define the figure of merits. We start with the volume-averaged β

$$\langle \beta \rangle = \frac{1}{\int_0^1 \oint \oint \sqrt{g} d\rho d\theta d\zeta} \int_0^1 \oint \oint \sqrt{g} d\rho d\theta d\zeta \frac{2\mu_0 p}{B^2}. \quad (\text{D.9})$$

Next, we define another important quantity of interest, the toroidal magnetic flux enclosed by the plasma boundary

$$\Psi_b = \int_0^1 \oint \oint \sqrt{g} d\rho d\theta d\zeta \mathbf{B} \cdot \nabla \zeta. \quad (\text{D.10})$$

and finally, the total enclosed toroidal plasma current

$$I_b = \frac{1}{2\pi\mu_0} \oint \oint d\theta d\zeta \mathbf{B} \cdot \frac{\partial \mathbf{x}}{\partial \theta}, \quad (\text{D.11})$$

where all the elements in the integrand and the integrals are calculated on the boundary.

Appendix E. Characterizing gyrokinetic modes

In this Appendix, we will explain how to characterize and separate different unstable modes from the output of an initial value gyrokinetic solver such as **GS2**. We will also provide details of the **GS2** runs used to calculate the maximum KBM growth rates in Section 6.

Appendix E.1. Separating KBMs from other microinstabilities

To obtain the maximum growth rate, we require a method to separate Kinetic Ballooning Modes (KBM) from other gyrokinetic instabilities such as the Ion Temperature Gradient (ITG) mode, Trapped Electron Mode (TEM), Microtearing mode (MTM), and the Electron Temperature Gradient (ETG) mode. To this end, we use a set of classification rules with which we can find the most unstable KBMs. To define these rules, we first define the quasilinear particle flux and heat flux

$$\Gamma_s = \left\langle \int d^3v \mathbf{V}_E \cdot \frac{\nabla\psi}{|\nabla\psi|} \right\rangle_\psi = \frac{a_N}{L_{ns}} D_s, \quad (\text{E.1})$$

$$q_s = \left\langle \int d^3v \mathbf{V}_E \cdot \frac{\nabla\psi}{|\nabla\psi|} \right\rangle_\psi = \frac{a_N}{L_{Ts}} \chi_s + \frac{3}{2} \Gamma_s, \quad (\text{E.2})$$

where the $\mathbf{E} \times \mathbf{B}$ drift \mathbf{V}_E is defined in (12), the gradient scale lengths a_N/L_{ns} , a_N/L_{Ts} are defined in (19), and χ_s and D_s are the heat and particle diffusivities, respectively. The operator

$$\langle X \rangle_\psi = \frac{\int \int d\theta d\zeta \sqrt{g} X}{\int \int d\theta d\zeta \sqrt{g}} \quad (\text{E.3})$$

is the flux surface averaging operator. We also define the parity of the gyrokinetic parallel vector potential δA_\parallel

$$\mathcal{P} = 1 - \frac{|\int d\theta \delta A_\parallel|}{\int d\theta |\delta A_\parallel|}. \quad (\text{E.4})$$

Using these classifying variables and the prescription provided in Table 1 of Parisi *et al.* [55, 56], we create table Appendix E.2 to separate KBM from the rest of the modes in the output produced by GS2.

Table E1: Characterizing various gyrokinetic modes

Mode	χ_i/χ_e	D_e/χ_e	D_i/χ_i	$\mathcal{P}(A_\parallel)$	$\partial\gamma/\partial\beta$
KBM	~ 1	~ 1	~ 1	1	> 0
TEM	~ 1	~ 1	—	1	< 0
ITG	$\gg 1$	—	$\ll 1$	1	< 0
ETG	$\ll 1$	$\ll 1$	—	1	< 0
MTM	$\ll 1$	$\ll 1$	—	< 1	> 0
EM-ETG	$\ll 1$	$\ll 1$	—	1	> 0

Appendix E.2. Details of GS2 runs

On each flux surface a GS2 simulation scans $N_\alpha = 8$ fieldlines. For each fieldline, we scan $N_{k_y} = 8$ values of the binormal wavenumber linearly spaced between the $k_y \in [0.05, 1.2]$ and $N_{k_x} = 12$ values of the radial wavenumbers linearly spaced between

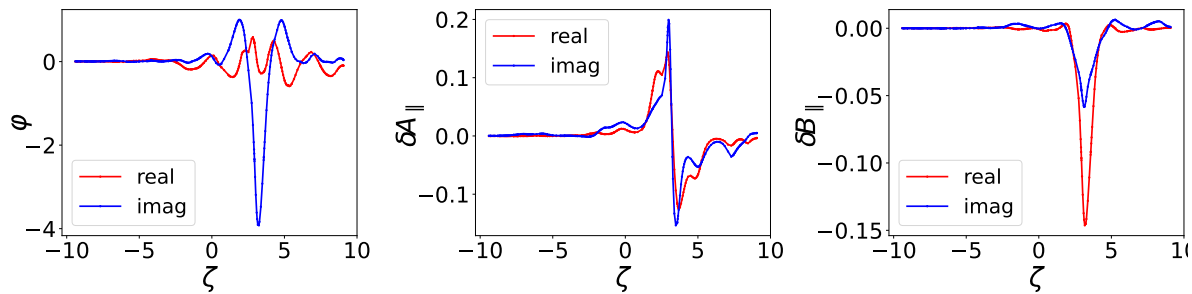


Figure E1: The set of eigenfunctions for the most unstable mode for the the initial OT equilibrium at $\rho = 1.0$. The peak growth rate occurs at $\alpha = 0, k_x = 1.2, k_y = 0.4$. Note the odd parity of the δA_{\parallel} , signature of a KBM.

$k_x \in [-\pi/(2\hat{s}), \pi/(2\hat{s})]$. The number of grid points along a flux tube is determined by the pitch angle resolution N_{λ} for which we choose $N_{\lambda} \geq 45$. The pitch angle resolution is sensitive to the type of omnigenity. In general OP equilibria require a higher N_{λ} and OT equilibria require the lowest N_{λ} . The resolution of the velocity space in GS2 is $n_{\text{gauss}} = 6, n_{\text{grid}} = 12$. Upon imposing all the criteria from table we can separate out the KBMs from the rest of the unstable modes. A typical set of eigenfunctions corresponding to the KBM are provided in figure E1.

Appendix F. Supplementary material

In this supplementary document, we will present the process by which the KBM equation can be simplified to the ideal ballooning equation.

Using the intermediate frequency ordering and subsidiary ordering neglecting the trapped particle effects presented in the Appendix of the main paper, we are left with three decoupled Ordinary Differential Equations (ODEs).

$$\phi = \hat{\psi}_{\parallel}, \quad (\text{F.1})$$

$$\delta\tilde{B}_{\parallel} = \frac{\beta_i}{2}\hat{\psi}_{\parallel}, \quad (\text{F.2})$$

$$\frac{1}{\sqrt{g}B} \frac{\partial}{\partial\zeta} \left(\frac{b}{\sqrt{g}B} \frac{\partial\hat{\psi}_{\parallel}}{\partial\zeta} \right) = \frac{\omega^2}{\omega_A^2} \hat{\psi}_{\parallel} K \quad (\text{F.3})$$

where

$$\sqrt{g} = [(\nabla\psi \times \nabla\theta) \cdot \nabla\zeta]^{-1} = \frac{1}{\mathbf{B} \cdot \nabla\zeta} \quad (\text{F.4})$$

$$\omega_A = \frac{v_A}{a_N}, \quad v_A = \frac{B_N}{\sqrt{4\pi\rho_0}} \quad (\text{F.5})$$

$$b = \frac{k_{\perp}^2 \rho_i^2}{2}, \quad \rho_i = \frac{w_{\text{th},i}}{\Omega_i}, \quad v_{\text{th},i} = \sqrt{\frac{2T_i}{m_i}}, \quad \Omega_i = \frac{eB}{m_i c} \quad (\text{F.6})$$

$$K = \left\{ \left[Q - \left(1 - \frac{\omega_{*e}}{\omega\tau} \right) \right] \left[\alpha_{0e} \left(1 + \frac{\beta_i}{2} R \right) - \alpha_{1e} \tau Q' \frac{\beta_i}{2} \right] \right. \quad (\text{F.7})$$

$$\left. - \frac{\beta_i}{2} (Q' + \alpha_{1e}) \left[\alpha_{0e} Q' + \alpha_{1e} (1 + \tau_e - \tau_e Q) \right] \right\} \quad (\text{F.8})$$

$$\left[(1 + \tau_e - \tau_e Q) \left(1 + \frac{\beta_i}{2} R \right) + \tau_e Q'^2 \frac{\beta_i}{2} \right]^{-1} - \alpha_{1e} \frac{\omega_{\kappa} + \omega_B}{\omega} \quad (\text{F.9})$$

$$\tau_e = 1, \quad \beta_i = \frac{8\pi p_i}{B^2} \quad (\text{F.10})$$

$$\alpha_{ls} = \left[1 - \frac{\omega_{*s}}{\omega} (1 + l\eta_s) \right], \quad \omega_{*s} = \frac{k_y \rho_s v_{\text{th},s}}{2 L_{n,s}} \tilde{B}, \quad (\text{F.11})$$

$$\eta_s = \frac{L_{n,s}}{L_{T,s}}, \quad \frac{a_N}{L_{T,s}} = \frac{1}{T_s} \frac{dT_s}{d\rho}, \quad \frac{a_N}{L_{n,s}} = \frac{1}{n_s} \frac{dn_s}{d\rho} \quad (\text{F.12})$$

$$\omega_{\kappa} = \omega_d (\mathbf{b} \times (\mathbf{b} \cdot \nabla_N \mathbf{b}) \cdot \nabla_N \alpha), \quad \omega_B = \omega_d (\mathbf{b} \times \nabla_N B \cdot \nabla_N \alpha), \quad \omega_d = \frac{k_y \rho_s}{2} \frac{v_{\text{th},s}}{L_{n,s}} \quad (\text{F.13})$$

$$\omega_{Di} = 2v_{\parallel,N}^2 \omega_{\kappa} + v_{\perp,N}^2 \omega_B = E [2(1 - \lambda B) \omega_{\kappa} + \lambda B \omega_B] \quad (\text{F.14})$$

$$F_{0s} = \frac{n_s}{(2\pi)^{3/2} v_{\text{th},i}^3} \exp \left(-\frac{(v_{\parallel}^2 + v_{\perp}^2)}{2} \right) = \frac{n_s}{(2\pi)^{3/2} v_{\text{th},i}^3} \exp \left(-\frac{v^2}{2} \right) \quad (\text{F.15})$$

$$Q = \int d^3\mathbf{v} \frac{F_{i0}}{n_0} J_0^2 \left(\frac{k_{\perp} v_{\perp}}{\Omega_i} \right) \left(\frac{\omega - \omega_{*i}^T}{\omega - \omega_{Di}} \right) \quad (\text{F.16})$$

$$Q' = \int d^3\mathbf{v} \frac{F_{0i}}{n_0} \frac{d}{db} \left[J_0^2 \left(\frac{k_\perp v_\perp}{\Omega_i} \right) \right] \left(\frac{\omega - \omega_{*i}^T}{\omega - \omega_{Di}} \right) \quad (\text{F.17})$$

$$R = \frac{2}{b} \int d^3\mathbf{v} \frac{F_{0i}}{n_0} v_\perp^2 J_1^2 \left(\frac{k_\perp v_\perp}{\Omega_i} \right) \left(\frac{\omega - \omega_{*i}^T}{\omega - \omega_{Di}} \right) \quad (\text{F.18})$$

$$\omega_{*,s}^T = \omega_{*,s} \left[1 + \eta_s \left(\frac{E}{T_s} - \frac{3}{2} \right) \right] \quad (\text{F.19})$$

Note that all the velocities have been normalized to $v_{\text{th},i} = \sqrt{2T_i/m_i}$. The resonant denominator in the expressions for Q, Q', R can be simplified

$$\frac{1}{\omega - \omega_D} = -i \int_0^\infty d\tau e^{i(\omega - \omega_D)\tau}, \quad \text{Im}(\omega) > 0 \quad (\text{F.20})$$

using Feynman's technique used for path integral formulation of quantum mechanics [57]. Since all the resonant denominators are inside velocity space integrals, we use a modified generating function, similar to the one defined by Biglari et. al [58] as

$$F_{\alpha,\beta} = -\frac{i}{(\pi)^{1/2}} \int_0^\infty d\tau \int_0^\infty d\omega_\perp^2 \int_{-\infty}^\infty d\omega_\parallel e^{\{-\alpha\omega_\parallel^2 - \beta\omega_\perp^2 + i\tau[\omega - (\omega_B\omega_\perp^2 + 2\omega_\kappa\omega_\parallel^2)]\}} \quad (\text{F.21})$$

$$= -i \int_0^\infty d\tau \frac{e^{i\omega\tau}}{(\alpha + 2i\omega_{\kappa,s}\tilde{\tau})^{1/2}(\beta + i\omega_{B,s}\tau)}, \quad (\text{F.22})$$

$$= -\frac{i}{\omega_{B,s}} \int_0^\infty d\tilde{\tau} \frac{e^{i\tilde{\omega}\tilde{\tau}}}{(\alpha + 2i\kappa\tilde{\tau})^{1/2}(\beta + i\tilde{\tau})}, \quad \kappa = \frac{\omega_{\kappa,s}}{\omega_{B,s}}, \tilde{\omega} = \frac{\omega}{\omega_{B,s}}, \tilde{\tau} = \tau\omega_{B,s} \quad (\text{F.23})$$

we have rewritten $\omega_{Ds} = E_s [(1 - \lambda B)\omega_{\kappa,s} + \lambda B\omega_{B,s}]$, $\omega_{\kappa,s} = (\mathbf{b} \times \boldsymbol{\kappa}) \cdot \mathbf{k}_\perp / B^2$, $\omega_{B,s} = (\mathbf{b} \times \nabla B \cdot \mathbf{k}_\perp) / B^2$ are the geometric factors in curvature and grad-B drifts, respectively. Equation (F.22) is the unnormalized form of $F_{\alpha,\beta}$ whereas (F.23) is the normalized form. The function F is defined such that

$$F_{1,1} = \int d^3\mathbf{v} \frac{F_{0s}}{\omega - \omega_{Ds}} = -\frac{i}{\pi^{1/2}} \int_0^\infty d\tilde{\tau} \frac{e^{i\omega\tilde{\tau}}}{(1 + 2i\omega_{\kappa,s}\tilde{\tau})^{1/2}(1 + i\omega_{B,s}\tilde{\tau})}, \quad (\text{F.24})$$

All terms in K in (F.3) can be calculated using $F_{\alpha,\beta}$ and its derivatives with respect to α and β . Moreover, all derivatives of the type $\partial_\alpha^i \partial_\beta^j F_{\alpha,\beta}$ can be obtained recursively from $F_{\alpha,\beta}$. An alternative form of $F_{\alpha,\beta}$ that we shall use is

$$F_{\alpha,\beta} = \frac{e^{-\beta\tilde{\omega}}}{(2\kappa)^{1/2}\omega_B} \int_{-\infty}^{\tilde{\omega}} dy y^{-1/2} e^{(\beta - \frac{\alpha}{2\kappa})y} \int_{-\infty}^{\frac{\alpha y}{2\kappa}} dz z^{-1/2} e^z. \quad (\text{F.25})$$

For arbitrary derivatives ∂_β of $F_{\alpha,\beta}$, we can obtain the following recursive relation

$$\partial_\beta^n F_{\alpha,\beta} = - \left[\tilde{\omega} + \frac{1}{2(\beta - \frac{\alpha}{2\kappa})} \right] \partial_\beta^{n-1} F_{\alpha,\beta} + \sum_{i=1, n>1}^{n-1} {}_{n-1}P_i \frac{(-1)^{i+1} \partial_\beta^{n-i-1} F_{\alpha,\beta}}{2(\beta - \frac{\alpha}{2\kappa})^{i+1}} \quad (\text{F.26})$$

$$+ (-1)^n \frac{\tilde{\omega}^{1/2}}{(2\kappa)^{1/2}\omega_B} Z \left(\sqrt{\frac{\alpha\tilde{\omega}}{2\kappa}} \right) \frac{(n-1)!}{(\beta - \frac{\alpha}{2\kappa})^n} + \frac{(-1)^{n-1}(n-1)!}{(2\kappa)^{1/2}\omega_B} \left[\frac{1}{\beta^n} - \frac{1}{(\beta - \frac{\alpha}{2\kappa})^n} \right] \quad (\text{F.27})$$

This calculation would have to be done serially, starting with $F_{\alpha,\beta}$ and then going to the required derivative. Next, we calculate the derivative with respect to α

$$\partial_\alpha F_{\alpha,\beta} = \frac{1}{(2\kappa)\omega_B \alpha^{1/2}\beta} - \frac{1}{2\kappa} (\partial_\beta F_{\alpha,\beta} + \tilde{\omega} F_{\alpha,\beta}) \quad (\text{F.28})$$

where we have used (F.25) to simplify the relation. Using this relation,

$$\partial_\beta \partial_\alpha F_{\alpha,\beta} = \partial_\alpha \partial_\beta F_{\alpha,\beta} = -\frac{1}{(2\kappa)\omega_d \alpha^{1/2}\beta^2} - \frac{1}{2\kappa} (\partial_\beta^2 F_{\alpha,\beta} + \tilde{\omega} \partial_\beta F_{\alpha,\beta}) \quad (\text{F.29})$$

Using the above relation, we can obtain a the following recursive relation

$$\partial_\beta^n \partial_\alpha F_{\alpha,\beta} = (-1)^n \frac{(n-1)!}{(2\kappa)\omega_B \alpha^{1/2}\beta^{n+1}} - \frac{1}{2\kappa} (\partial_\beta^{n+1} F_{\alpha,\beta} + \tilde{\omega} \partial_\beta^n F_{\alpha,\beta}) \quad (\text{F.30})$$

Unlike the partial derivatives with respect to β , we will never need α derivatives beyond the second order. The second order derivative with respect to α is

$$\begin{aligned} \partial_\alpha^2 F_{\alpha,\beta} &= -\frac{1}{2(2\kappa)\omega_B \alpha^{3/2}\beta} - \frac{1}{2\kappa} (\partial_\beta \partial_\alpha F_{\alpha,\beta} + \tilde{\omega} \partial_\alpha F_{\alpha,\beta}) \\ &= -\frac{1}{2(2\kappa)\omega_B \alpha^{3/2}\beta^2} \left(\beta + \frac{\tilde{\omega}\alpha\beta}{\kappa} - \frac{\alpha}{\kappa} \right) + \frac{1}{(2\kappa)^2} (\partial_\beta + \tilde{\omega})^2 F_{\alpha,\beta} \end{aligned} \quad (\text{F.31})$$

Using the various definitions of $F_{\alpha,\beta}$, we can simplify the terms Q , Q^1 , and R as presented in this section

Appendix F.1. Simplified velocity integrals

$$\begin{aligned} Q &= -\frac{i}{(\pi)^{1/2}\omega_B} \int_0^\infty d\tilde{\tau} \int_{-\infty}^\infty dw_\parallel \int_0^\infty dw_\perp^2 J_0^2 \left(\frac{k_\perp w_\perp}{\Omega_i} \right) \\ &\quad \left\{ \tilde{\omega} - \omega_{*,j} \left[1 + \eta \left(\frac{E}{T} - \frac{3}{2} \right) \right] \right\} e^{i[\tilde{\omega} - (w_\perp^2 + 2\kappa w_\parallel^2)]\tilde{\tau}} e^{-(w_\perp^2 + w_\parallel^2)}, \end{aligned} \quad (\text{F.32})$$

The velocity integrals can be calculated analytically exactly. Using MATHEMATICA[®] [59], we evaluate the following simpler sub-integrals

$$\begin{aligned} Q_1 &= \frac{1}{(\pi)^{1/2}} \int_{-\infty}^\infty dw_\parallel e^{-w_\parallel^2(1+2i\kappa\tilde{\tau})} \int_0^\infty dw_\perp^2 J_0^2 e^{-w_\perp^2(1+i\tau)} \\ &= \frac{1}{\sqrt{1+2i\kappa\tau}} \frac{e^{-\left(\frac{b}{1+i\tau}\right)}}{1+i\tau} I_0 \left(\frac{b}{1+i\tau} \right) \\ &= \frac{1}{\sqrt{1+2i\kappa\tau}} \left[\frac{1}{1+i\tau} - \frac{b}{(1+i\tau)^2} \right] + \mathcal{O}(k_\perp^4 \rho_i^4) \\ &= F_{\alpha,\beta} - b \partial_\beta F_{\alpha,\beta} + \mathcal{O}(k_\perp^4 \rho_i^4) \end{aligned} \quad (\text{F.33})$$

$$\begin{aligned} Q_2 &= \frac{1}{(\pi)^{1/2}} \int_{-\infty}^\infty dw_\parallel e^{-w_\parallel^2(1+2i\kappa\tau)} \int_0^\infty dw_\perp^2 w_\perp^2 J_0^2 e^{-w_\perp^2(1+i\tau)} \\ &= \frac{1}{\sqrt{1+2i\kappa\tau}} \frac{e^{-\left(\frac{b}{1+i\tau}\right)}}{(1+i\tau)^3} \left[(1+i\tau-b) I_0 \left(\frac{b}{1+i\tau} \right) + b I_1 \left(\frac{b}{1+i\tau} \right) \right] \\ &= \frac{1}{\sqrt{1+2i\kappa\tau}} \left[\frac{1}{(1+i\tau)^2} - \frac{2b}{(1+i\tau)^3} \right] + \mathcal{O}(k_\perp^4 \rho_i^4) \\ &= -(\partial_\beta F_{\alpha,\beta} - b \partial_\beta^2 F_{\alpha,\beta}) + \mathcal{O}(k_\perp^4 \rho_i^4) \end{aligned} \quad (\text{F.34})$$

$$\begin{aligned}
Q_3 &= \frac{1}{(\pi)^{1/2}} \int_{-\infty}^{\infty} dw_{\parallel} w_{\parallel}^2 e^{-w_{\parallel}^2(1+2i\kappa\tau)} \int_0^{\infty} dw_{\perp}^2 J_0^2 e^{-w_{\perp}^2(1+i\tau)} \\
&= \frac{1}{2(1+2i\kappa\tau)^{3/2}} \frac{e^{-\left(\frac{b}{1+i\tau}\right)}}{1+i\tau} I_0 \left(\frac{b}{1+i\tau} \right) \\
&= \frac{1}{2(1+2i\kappa\tau)^{3/2}} \left[\frac{1}{1+i\tau} - \frac{b}{(1+i\tau)^2} \right] + \mathcal{O}(k_{\perp}^4 \rho_i^4) \\
&= -(\partial_{\alpha} F_{\alpha,\beta} + b \partial_{\alpha} \partial_{\beta} F_{\alpha,\beta})
\end{aligned} \tag{F.35}$$

Combining Q_1, Q_2 and Q_3 , we can write

$$\begin{aligned}
Q &= -\frac{i}{\omega_B} \int_0^{\infty} d\tilde{\tau} e^{(i\tilde{\omega}\tau)} \left[\left(\tilde{\omega} - \omega_{*,j} + \frac{3}{2}\eta\omega_{*,j} \right) Q_1 - \eta\omega_{*,j}(Q_2 + Q_3) \right] \\
&= \left[\left(\tilde{\omega} - \omega_{*,j} + \frac{3}{2}\eta\omega_{*,j} \right) (1 + b\partial_{\beta}) F_{\alpha,\beta} \right. \\
&\quad \left. + \eta\omega_{*,j}((\partial_{\beta} + b\partial_{\beta}^2)F_{\alpha,\beta} + \partial_{\alpha}(1 + b\partial_{\beta})F_{\alpha,\beta}) \right] \Big|_{\alpha=1,\beta=1} + \mathcal{O}((k_{\perp}\rho_i)^4)
\end{aligned} \tag{F.36}$$

The next term Q' is

$$\begin{aligned}
Q' &= -\frac{i}{(\pi)^{1/2}\omega_B} \int_0^{\infty} d\tilde{\tau} \int_{-\infty}^{\infty} dw_{\parallel} \int_0^{\infty} dw_{\perp}^2 \frac{d}{db} \left[J_0^2 \left(\frac{k_{\perp} w_{\perp}}{\Omega_i} \right) \right] \\
&\quad \left\{ \tilde{\omega} - \omega_{*,j} \left[1 + \eta \left(\frac{E}{T} - \frac{3}{2} \right) \right] \right\} e^{i(\tilde{\omega} - (w_{\perp}^2 + 2\kappa w_{\parallel}^2))\tau} e^{-(w_{\perp}^2 + w_{\parallel}^2)}
\end{aligned} \tag{F.37}$$

The corresponding sub-integrals are

$$\begin{aligned}
Q'_1 &= \frac{1}{\pi^{1/2}} \int_{-\infty}^{\infty} dw_{\parallel} e^{-(w_{\parallel}^2(1+2i\tau))} \int_0^{\infty} dw_{\perp}^2 \frac{k_{\perp}\rho_i}{b}(w_{\perp}) J_0 J_0' e^{-w_{\perp}^2(1+i\tau)} \\
&= -\frac{1}{\sqrt{1+2i\kappa\tau}} \frac{e^{-\left(\frac{b}{1+i\tau}\right)}}{(1+i\tau)^2} \left[I_0 \left(\frac{b}{1+i\tau} \right) - I_1 \left(\frac{b}{1+i\tau} \right) \right] \\
&= -\frac{1}{\sqrt{1+2i\kappa\tau}} \left[\frac{1}{(1+i\tau)^2} - \frac{3b}{2(1+i\tau)^3} \right] + \mathcal{O}(k_{\perp}^4 \rho_i^4) \\
&= \partial_{\beta} F_{\alpha,\beta} + \frac{3}{4} \partial_{\beta}^2 F_{\alpha,\beta} + \mathcal{O}((k_{\perp}\rho_i)^4)
\end{aligned} \tag{F.38}$$

$$\begin{aligned}
Q'_2 &= \frac{1}{\pi^{1/2}} \int_{-\infty}^{\infty} dw_{\parallel} e^{-w_{\parallel}^2(1+2i\tau)} \int_0^{\infty} dw_{\perp}^2 w_{\perp}^2 \frac{k_{\perp}\rho_i}{b}(w_{\perp}) J_0 J_0' e^{-w_{\perp}^2(1+i\tau)} \\
&= \frac{2}{\sqrt{1+2i\kappa\tau}} \frac{e^{-\left(\frac{b}{1+i\tau}\right)}}{(1+i\tau)^4} \left[(b - (1+i\tau)) I_0 \left(\frac{b}{1+i\tau} \right) + (0.5(1+i\tau) - b) I_1 \left(\frac{b}{1+i\tau} \right) \right] \\
&= \frac{1}{\sqrt{1+2i\kappa\tau}} \left[-\frac{2}{(1+i\tau)^3} + \frac{9}{4} \frac{2b}{(1+i\tau)^4} \right] + \mathcal{O}((k_{\perp}\rho_i)^4) \\
&= -\left(\partial_{\beta}^2 F_{\alpha,\beta} + \frac{3}{4} \partial_{\beta}^3 F_{\alpha,\beta} \right) + \mathcal{O}((k_{\perp}\rho_i)^4)
\end{aligned} \tag{F.39}$$

$$\begin{aligned}
Q'_3 &= \frac{1}{\pi^{1/2}} \int_{-\infty}^{\infty} dw_{\parallel} w_{\parallel}^2 e^{-w_{\parallel}^2(1+2i\tau)} \int_0^{\infty} dw_{\perp}^2 \frac{k_{\perp} \rho_i}{b} (w_{\perp}) J_0 J'_0 e^{-w_{\perp}^2(1+i\tau)} \\
&= -\frac{1}{2(1+2i\kappa\tau)^{3/2}} \frac{e^{-\left(\frac{b}{1+i\tau}\right)}}{(1+i\tau)^2} \left[I_0 \left(\frac{b}{1+i\tau} \right) - I_1 \left(\frac{b}{1+i\tau} \right) \right] \\
&= -\frac{1}{2(1+2i\kappa\tau)^{3/2}} \left[\frac{1}{(1+i\tau)^2} - \frac{3}{2} \frac{b}{(1+i\tau)^3} \right] \\
&= -\left(\partial_{\alpha} \partial_{\beta} F_{\alpha,\beta} + \frac{3}{4} \partial_{\alpha} \partial_{\beta}^2 F_{\alpha,\beta} \right) + \mathcal{O}((k_{\perp} \rho_i)^4)
\end{aligned} \tag{F.40}$$

Combining Q'_1, Q'_2, Q'_3 , we can write

$$Q' = -\frac{i}{\omega_B} \int_0^{\infty} d\tilde{\tau} e^{i\tilde{\omega}\tau} \left[\left(\tilde{\omega} - \omega_{*,j} + \frac{3}{2} \eta \omega_{*,j} \right) Q'_1 - \eta \omega_{*,j} (Q'_2 + Q'_3) \right], \tag{F.41}$$

which using the generating function $F_{\alpha,\beta}$ can be written as

$$\begin{aligned}
Q' &= \left\{ \left(\tilde{\omega} - \omega_{*,j} + \frac{3}{2} \eta \omega_{*,j} \right) \left(\partial_{\beta} + \frac{3}{4} b \partial_{\beta}^2 \right) F_{\alpha,\beta} \right. \\
&\quad \left. + \eta \omega_{*,j} \left[\left(\partial_{\beta}^2 F_{\alpha,\beta} + \frac{3}{4} b \partial_{\beta}^3 \right) + \partial_{\alpha} \left(\partial_{\beta} + \frac{3}{4} b \partial_{\beta}^2 \right) F_{\alpha,\beta} \right] \right\} \Big|_{\alpha=1,\beta=1} + \mathcal{O}((k_{\perp} \rho_i)^4)
\end{aligned} \tag{F.42}$$

The corrected R term

$$\begin{aligned}
\tilde{R} &= -\frac{2i}{\sqrt{\pi} \omega_B} \int_0^{\infty} d\tau \int_{-\infty}^{\infty} dw_{\parallel} \int_0^{\infty} dw_{\perp}^2 \frac{w_{\perp}^2}{b} J_1^2 \left(\frac{k_{\perp} w_{\perp}}{\Omega_i} \right) \\
&\quad \left\{ \omega - \omega_{*,j} \left[1 + \eta \left(\frac{E}{T} - \frac{3}{2} \right) \right] \right\} e^{i(\tilde{\omega} - (w_{\perp}^2 + 2\kappa w_{\parallel}^2))\tau} e^{-(w_{\perp}^2 + w_{\parallel}^2)}
\end{aligned} \tag{F.43}$$

The term \tilde{R} can be split into

$$\begin{aligned}
\tilde{R}_1 &= \frac{2}{\sqrt{\pi}} \int_{-\infty}^{\infty} dw_{\parallel} e^{-w_{\parallel}^2(1+2i\tau)} \int_0^{\infty} dw_{\perp}^2 \left(\frac{w_{\perp}^2}{b} \right) J_1^2 e^{-w_{\perp}^2(1+i\tau)} \\
&= \frac{2}{\sqrt{1+2i\kappa\tau}} \frac{e^{-\left(\frac{b}{1+i\tau}\right)}}{(1+i\tau)^3} \left[I_0 \left(\frac{b}{1+i\tau} \right) - I_1 \left(\frac{b}{1+i\tau} \right) \right] \\
&= \frac{2}{\sqrt{1+2i\kappa\tau}} \left[\frac{1}{(1+i\tau)^3} - \frac{3b}{2(1+i\tau)^4} \right] \\
&= \left(\partial_{\beta}^2 F_{\alpha,\beta} + \frac{b}{2} \partial_{\beta}^3 F_{\alpha,\beta} \right) + \mathcal{O}((k_{\perp} \rho_i)^2)
\end{aligned} \tag{F.44}$$

Next, we write

$$\begin{aligned}
\tilde{R}_2 &= \frac{2}{\sqrt{\pi}} \int_{-\infty}^{\infty} dw_{\parallel} e^{-w_{\parallel}^2(1+2i\tau)} \int_0^{\infty} dw_{\perp}^2 \left(\frac{w_{\perp}^4}{b} \right) J_1^2 e^{-w_{\perp}^2(1+i\tau)} \\
&= \frac{2}{\sqrt{1+2i\kappa\tau}} \frac{e^{-\left(\frac{b}{1+i\tau}\right)}}{(1+i\tau)^5} \left[(3(1+i\tau) - 2b) I_0 \left(\frac{b}{1+i\tau} \right) - 2(1+i\tau - b) I_1 \left(\frac{b}{1+i\tau} \right) \right] \\
&= \frac{6}{\sqrt{1+2i\kappa\tau}} \left[\frac{1}{(1+i\tau)^4} - \frac{2b}{(1+i\tau)^5} \right] \\
&= -\left(\partial_{\beta}^3 F_{\alpha,\beta} + \frac{b}{2} \partial_{\beta}^4 F_{\alpha,\beta} \right)
\end{aligned} \tag{F.45}$$

The third term

$$\begin{aligned}
\tilde{R}_3 &= \frac{2}{\sqrt{\pi}} \int_{-\infty}^{\infty} dw_{\parallel} w_{\parallel}^2 e^{-w_{\parallel}^2(1+2i\tau)} \int_0^{\infty} dw_{\perp}^2 \left(\frac{w_{\perp}^2}{b} \right) J_1^2 e^{-w_{\perp}^2(1+i\tau)} \\
&= \frac{2}{2(\sqrt{1+2i\kappa\tau})^3 (1+i\tau)^3} \left[I_0 \left(\frac{b}{1+i\tau} \right) - I_1 \left(\frac{b}{1+i\tau} \right) \right] \\
&= - \left(\partial_{\alpha} \partial_{\beta}^2 F_{\alpha,\beta} + \frac{b}{2} \partial_{\alpha} \partial_{\beta}^3 F_{\alpha,\beta} \right)
\end{aligned} \tag{F.46}$$

Combining \tilde{R}_1 , \tilde{R}_2 and \tilde{R}_3 , we get

$$\begin{aligned}
\tilde{R} &= -\frac{i}{\omega_B} \int_0^{\infty} d\tilde{\tau} e^{i\omega\tau} \left[\left(\omega - \omega_{*,j} + \frac{3}{2}\eta\omega_{*,j} \right) \tilde{R}_1 - \eta\omega_{*,j} (\tilde{R}_2 + \tilde{R}_3) \right] \\
&= \left\{ \left(\omega - \omega_{*,j} + \frac{3}{2}\eta\omega_{*,j} \right) \left(\partial_{\beta}^2 + \frac{b}{2}\partial_{\beta}^3 \right) F_{\alpha,\beta} \right. \\
&\quad \left. + \eta\omega_{*,j} \left[\left(\partial_{\beta}^3 + \frac{b}{2}\partial_{\beta}^4 \right) + \partial_{\alpha} \left(\partial_{\beta}^2 + \frac{b}{2}\partial_{\beta}^3 \right) \right] F_{\alpha,\beta} \right\} \Big|_{\alpha=1,\beta=1}
\end{aligned} \tag{F.47}$$

Finally, we can write the resonant integrals as

$$\begin{aligned}
Q &= \left[\left(\tilde{\omega} - \omega_{*,j} + \frac{3}{2}\eta\omega_{*,j} \right) (1 + b\partial_{\beta}) F_{\alpha,\beta} \right. \\
&\quad \left. + \eta\omega_{*,j} ((\partial_{\beta} + b\partial_{\beta}^2) F_{\alpha,\beta} + \partial_{\alpha} (1 + b\partial_{\beta}) F_{\alpha,\beta}) \right] \Big|_{\alpha=1,\beta=1} + \mathcal{O}(k_{\perp}^4 \rho_i^4) \\
Q' &= \left\{ - \left(\tilde{\omega} - \omega_{*,j} + \frac{3}{2}\eta\omega_{*,j} \right) \left(\partial_{\beta} + \frac{3}{2}b\partial_{\beta}^2 \right) F_{\alpha,\beta} \right. \\
&\quad \left. - \eta\omega_{*,j} \left[(b\partial_{\beta} - 2\partial_{\beta}^2) F_{\alpha,\beta} + \partial_{\alpha} \left(-\frac{1}{2}\partial_{\beta} + b\partial_{\beta}^2 \right) F_{\alpha,\beta} \right] \right\} \Big|_{\alpha=1,\beta=1} \\
\tilde{R} &= \left\{ \left(\omega - \omega_{*,j} + \frac{3}{2}\eta\omega_{*,j} \right) \left(\partial_{\beta}^2 + \frac{b}{2}\partial_{\beta}^3 \right) F_{\alpha,\beta} \right. \\
&\quad \left. + \eta\omega_{*,j} \left[\left(\partial_{\beta}^3 + \frac{b}{2}\partial_{\beta}^4 \right) + \partial_{\alpha} \left(\partial_{\beta}^2 + \frac{b}{2}\partial_{\beta}^3 \right) \right] F_{\alpha,\beta} \right\} \Big|_{\alpha=1,\beta=1}
\end{aligned} \tag{F.48}$$

where $F_{\alpha,\beta}(\theta, k_y \rho_i)$ and all the related derivatives can be calculated easily.

Appendix F.2. Further simplification

In this section of the Appendix, we will simplify the function $F_{\alpha,\beta}$ and compare the integrals Q, Q' and R with Aleynikova and Zocco's [50] analytical expressions. To simplify $F_{\alpha,\beta}$, we use subsidiary ordering by writing the denominator as a binomial series

$$(1 + 2i\omega_{\kappa,s}\tau)^{-1/2} = 1 - i\omega_{\kappa,s}\tau + 3/2(\omega_{\kappa,s}\tau)^2 + \dots \tag{F.49}$$

$$(1 + i\omega_{B,s}\tau)^{-1} = 1 - i\omega_{B,s}\tau - (\omega_{B,s}\tau)^2 + \dots \tag{F.50}$$

and calculate

$$F_{\alpha,\beta} = -i \int_0^{\infty} d\tau \frac{e^{i\omega\tau}}{(\alpha + 2i\omega_{\kappa,s}\tau)^{1/2} (\beta + i\omega_{B,s}\tau)}, \tag{F.51}$$

term by term. We can do the same for the derivatives of $F_{\alpha,\beta}$, with respect to α and β . Using the integral relations

$$\begin{aligned}\int_0^\infty e^{i\omega\tau} d\tau &= -\frac{1}{i\omega}, \\ \int_0^\infty \tau e^{i\omega\tau} d\tau &= -\frac{1}{\omega^2}, \\ \int_0^\infty \tau^2 e^{i\omega\tau} d\tau &= \frac{2}{i\omega^3}\end{aligned}\tag{F.52}$$

and the subsidiary ordering, we get, up to second order in δ

$$\begin{aligned}F_{\alpha,\beta} &= \left[\frac{1}{\omega} + \frac{(\omega_B + \omega_\kappa)}{\omega^2} + \frac{(3\omega_\kappa^2 + 2\omega_B^2 + 2\omega_\kappa\omega_B)}{\omega^3} \right] \\ \partial_\beta F_{\alpha,\beta} &= - \left[\frac{1}{\omega} + \frac{(2\omega_B + \omega_\kappa)}{\omega^2} + \frac{(3\omega_\kappa^2 + 6\omega_B^2 + 4\omega_\kappa\omega_B)}{\omega^3} \right] \\ \partial_\beta^2 F_{\alpha,\beta} &= 2! \left[\frac{1}{\omega} + \frac{(3\omega_B + \omega_\kappa)}{\omega^2} + \frac{(3\omega_\kappa^2 + 12\omega_B^2 + 6\omega_\kappa\omega_B)}{\omega^3} \right] \\ \partial_\beta^3 F_{\alpha,\beta} &= -3! \left[\frac{1}{\omega} + \frac{(4\omega_B + \omega_\kappa)}{\omega^2} + \frac{(3\omega_\kappa^2 + 20\omega_B^2 + 8\omega_\kappa\omega_B)}{\omega^3} \right] \\ \partial_\beta^4 F_{\alpha,\beta} &= 4! \left[\frac{1}{\omega} + \frac{(5\omega_B + \omega_\kappa)}{\omega^2} + \frac{(3\omega_\kappa^2 + 30\omega_B^2 + 8\omega_\kappa\omega_B)}{\omega^3} \right] \\ \partial_\alpha F_{\alpha,\beta} &= -\frac{1}{2} \left[\frac{1}{\omega} + \frac{(\omega_B + 3\omega_\kappa)}{\omega^2} + \frac{(15\omega_\kappa^2 + 2\omega_B^2 + 6\omega_\kappa\omega_B)}{\omega^3} \right] \\ \partial_\alpha \partial_\beta F_{\alpha,\beta} &= \frac{1}{2} \left[\frac{1}{\omega} + \frac{(2\omega_B + 3\omega_\kappa)}{\omega^2} + \frac{(15\omega_\kappa^2 + 6\omega_B^2 + 12\omega_\kappa\omega_B)}{\omega^3} \right] \\ \partial_\alpha \partial_\beta^2 F_{\alpha,\beta} &= -1 \left[\frac{1}{\omega} + \frac{(3\omega_B + 3\omega_\kappa)}{\omega^2} + \frac{(15\omega_\kappa^2 + 12\omega_B^2 + 18\omega_\kappa\omega_B)}{\omega^3} \right] \\ \partial_\alpha \partial_\beta^3 F_{\alpha,\beta} &= 2 \left[\frac{1}{\omega} + \frac{(4\omega_B + 3\omega_\kappa)}{\omega^2} + \frac{(15\omega_\kappa^2 + 20\omega_B^2 + 24\omega_\kappa\omega_B)}{\omega^3} \right] \\ \partial_\alpha \partial_\beta^4 F_{\alpha,\beta} &= -6 \left[\frac{1}{\omega} + \frac{(5\omega_B + 3\omega_\kappa)}{\omega^2} + \frac{(15\omega_\kappa^2 + 30\omega_B^2 + 30\omega_\kappa\omega_B)}{\omega^3} \right]\end{aligned}\tag{F.53}$$

Using the analytical expressions for different derivatives of the function $F_{\alpha,\zeta}$, we can simplify Q , Q' , and R .

$$\begin{aligned}Q &= \left[\left(\omega - \omega_{*,j} + \frac{3}{2}\eta\omega_{*,j} \right) (1 + b\partial_\beta) F_{\alpha,\beta} + \eta\omega_{*,j} ((\partial_\beta + b\partial_\beta^2) F_{\alpha,\beta} + \partial_\alpha(1 + b\partial_\beta) F_{\alpha,\beta}) \right] \Big|_{\alpha=\beta=1} \\ &= \left(1 - \frac{\omega_{*,j}}{\omega} \right) + \left(\frac{\omega_B + \omega_\kappa}{\omega} - \frac{(k_\perp \rho_i)^2}{2} \right) \left(1 - \frac{\omega_*}{\omega} (1 + \eta_{i,j}) \right) + \mathcal{O}(\delta^2)\end{aligned}\tag{F.54}$$

$$\begin{aligned}Q' &= \left\{ \left(\tilde{\omega} - \omega_{*,j} + \frac{3}{2}\eta\omega_{*,j} \right) \left(\partial_\beta + \frac{3}{4}b\partial_\beta^2 \right) F_{\alpha,\beta} \right. \\ &\quad \left. + \eta\omega_{*,j} \left[\left(\partial_\beta^2 F_{\alpha,\beta} + \frac{3}{4}b\partial_\beta^3 \right) + \partial_\alpha \left(\partial_\beta + \frac{3}{4}b\partial_\beta^2 \right) F_{\alpha,\beta} \right] \right\} \Big|_{\alpha=1,\beta=1} + \mathcal{O}((k_\perp \rho_i)^4) \\ &= - \left[1 - \frac{\omega_{*,j}}{\omega} (1 + \eta) \right] - \left[\frac{2\omega_B + \omega_\kappa}{\omega} + \frac{3}{4} \frac{(k_\perp \rho_i)^2}{2} \right] \left[\left(1 - \frac{\omega_{*,j}}{\omega} (1 + 2\eta) \right) \right] + \mathcal{O}(\delta^2)\end{aligned}\tag{F.55}$$

$$\begin{aligned}
\tilde{R} &= \left\{ \left(\omega - \omega_{*,j} + \frac{3}{2} \eta \omega_{*,j} \right) \left(\partial_\beta^2 + \frac{b}{2} \partial_\beta^3 \right) F_{\alpha,\beta} \right. \\
&+ \left. \eta \omega_{*,j} \left[\left(\partial_\beta^3 + \frac{b}{2} \partial_\beta^4 \right) + \partial_\alpha \left(\partial_\beta^2 + \frac{b}{2} \partial_\beta^3 \right) \right] F_{\alpha,\beta} \right\} \Big|_{\alpha=1, \beta=1}, \\
&= 2 \left[1 - \frac{\omega_{*,i}}{\omega} (1 + 2\eta) \right] + \mathcal{O}(\delta)
\end{aligned} \tag{F.56}$$

Higher-order terms have been omitted since all terms involving R in K are of order $\mathcal{O}(\delta^2)$ and thus are disregarded.

References

- [1] L. Spitzer Jr, “The stellarator concept,” *The Physics of Fluids*, vol. 1, pp. 253–264, 1958.
- [2] S. Lazerson, J. Schmitt, C. Zhu, J. Breslau, and A. [STELLOPT] Developers, “Stellopt,” may 2020.
- [3] M. Drevlak, C. D. Beidler, J. Geiger, P. Helander, and Y. Turkin, “Optimisation of stellarator equilibria with rose,” *Nuclear Fusion*, vol. 59, p. 016010, 2018.
- [4] M. Landreman, B. Medasani, F. Wechsung, A. Giuliani, R. Jorge, and C. Zhu, “SIMSOPT: A flexible framework for stellarator optimization,” *Journal of Open Source Software*, vol. 6, p. 3525, 2021.
- [5] S. P. Hirshman and J. C. Whitson, “Steepest-descent moment method for three-dimensional magnetohydrodynamic equilibria,” *The Physics of fluids*, vol. 26, p. 3553, 1983.
- [6] E. J. Paul, *Adjoint methods for stellarator shape optimization and sensitivity analysis*. PhD thesis, University of Maryland, College Park, 2020.
- [7] D. Panici, R. Conlin, D. W. Dudt, K. Unalmis, and E. Kolemen, “The desc stellarator code suite. part 1. quick and accurate equilibria computations,” *Journal of Plasma Physics*, vol. 89, p. 955890303, 2023.
- [8] D. Dudt and E. Kolemen, “Desc: A stellarator equilibrium solver,” *Physics of Plasmas*, vol. 27, no. 10, 2020.
- [9] R. Conlin, D. W. Dudt, D. Panici, and E. Kolemen, “The desc stellarator code suite. part 2. perturbation and continuation methods,” *Journal of Plasma Physics*, vol. 89, p. 955890305, 2023.
- [10] D. W. Dudt, R. Conlin, D. Panici, and E. Kolemen, “The desc stellarator code suite part 3: Quasi-symmetry optimization,” *Journal of Plasma Physics*, vol. 89, p. 955890201, 2023.
- [11] S. C. Cowley, R. M. Kulsrud, and R. Sudan, “Considerations of ion-temperature-gradient-driven turbulence,” *Phys. Fluids B*, vol. 3, p. 2767, 1991.
- [12] L. I. Rudakov and R. Z. Sagdeev, “On the instability of a nonuniform rarefied plasma in a strong magnetic field,” in *Doklady Akademii Nauk*, vol. 138, pp. 581–583, Russian Academy of Sciences, 1961.
- [13] J. Adam, W. Tang, and P. Rutherford, “Destabilization of the trapped electron mode by magnetic curvature drift resonances,” tech. rep., Princeton Plasma Physics Lab.(PPPL), Princeton, NJ (United States), 1975.
- [14] F. Ryter, C. Angioni, A. Peeters, F. Leuterer, H.-U. Fahrbach, W. Suttrop, and A. U. Team), “Experimental study of trapped-electron-mode properties in tokamaks: Threshold and stabilization by collisions,” *Physical review letters*, vol. 95, no. 8, p. 085001, 2005.
- [15] W. Tang, J. Connor, and R. Hastie, “Kinetic-ballooning-mode theory in general geometry,” *Nuclear Fusion*, vol. 20, no. 11, p. 1439, 1980.
- [16] W. D. D’haeseleer, W. N. G. Hitchon, J. D. Callen, and J. L. Shohet, *Flux coordinates and magnetic field structure: a guide to a fundamental tool of plasma theory*. Springer Science & Business Media, 2012.

- [17] J. M. Greene and M. S. Chance, “The second region of stability against ballooning modes,” *Nucl. Fusion*, vol. 21, p. 453, 1981.
- [18] C. Hegna and N. Nakajima, “On the stability of mercier and ballooning modes in stellarator configurations,” *Physics of Plasmas*, vol. 5, pp. 1336–1344, 1998.
- [19] S. R. Hudson, C. C. Hegna, R. Torasso, and A. Ware, “Marginal stability diagrams for infinite-n ballooning modes in quasi-symmetric stellarators,” *Plasma physics and controlled fusion*, vol. 46, no. 5, p. 869, 2004.
- [20] I. G. Abel, G. G. Plunk, E. Wang, M. Barnes, S. C. Cowley, W. Dorland, and A. A. Schekochihin, “Multiscale gyrokinetics for rotating tokamak plasmas: fluctuations, transport and energy flows,” *Reports on Progress in Physics*, vol. 76, p. 116201, 2013.
- [21] T. M. Antonsen Jr. and B. Lane, “Kinetic equations for low frequency instabilities in inhomogeneous plasmas,” *The Physics of Fluids*, vol. 23, p. 1205, 1980.
- [22] E. A. Frieman and L. Chen, “Nonlinear gyrokinetic equations for low-frequency electromagnetic waves in general plasma equilibria,” *Phys. Fluids*, vol. 25, p. 502, 1982.
- [23] M. Kotschenreuther, W. Dorland, M. A. Beer, and G. W. Hammett, “Quantitative predictions of tokamak energy confinement from first-principles simulations with kinetic effects,” *Phys. Plasmas*, vol. 2, p. 2381, 1995.
- [24] M. Kotschenreuther, G. W. Rewoldt, and W. M. Tang, “Comparison of initial value and eigenvalue codes for kinetic toroidal plasma instabilities,” *Comp. Phys. Comm.*, vol. 88, p. 128, 1995.
- [25] W. Dorland, F. Jenko, M. Kotschenreuther, and B. N. Rogers, “Electron temperature gradient turbulence,” *Phys. Rev. Lett.*, vol. 85, p. 5579, 2000.
- [26] F. Jenko, W. Dorland, M. Kotschenreuther, and B. N. Rogers, “Electron temperature gradient driven turbulence,” *Phys. Plasmas*, vol. 7, p. 1904, 2000.
- [27] C. Hegna and S. Hudson, “Loss of second-ballooning stability in three-dimensional equilibria,” *Physical Review Letters*, vol. 87, p. 035001, 2001.
- [28] R. Gaur, I. G. Abel, D. Dickinson, and W. D. Dorland, “Microstability of $\beta \sim 1$ tokamak equilibria,” *Journal of Plasma Physics*, vol. 89, no. 1, p. 905890112, 2023.
- [29] R. Gaur, S. Buller, M. E. Ruth, M. Landreman, I. G. Abel, and W. D. Dorland, “An adjoint-based method for optimising MHD equilibria against the infinite-n, ideal ballooning mode,” *Journal of Plasma Physics*, vol. 89, p. 905890518, 2023.
- [30] R. Sanchez, S. P. Hirshman, J. C. Whitson, and A. S. Ware, “COBRA: an optimized code for fast analysis of ideal ballooning stability of three-dimensional magnetic equilibria,” *Journal of Computational Physics*, vol. 161, p. 576, 2000.
- [31] L. S. Hall and B. McNamara, “Three-dimensional equilibrium of the anisotropic, finite-pressure guiding-center plasma: Theory of the magnetic plasma,” *The Physics of Fluids*, vol. 18, no. 5, pp. 552–565, 1975.
- [32] D. A. Garren and A. H. Boozer, “Magnetic field strength of toroidal plasma equilibria,” *Physics of Fluids B: Plasma Physics*, vol. 3, pp. 2805–2821, 1991.
- [33] J. R. Cary and S. G. Shasharina, “Helical plasma confinement devices with good confinement properties,” *Physical review letters*, vol. 78, p. 674, 1997.
- [34] G. G. Plunk, M. Landreman, and P. Helander, “Direct construction of optimized stellarator shapes. part 3. omnigenity near the magnetic axis,” *Journal of Plasma Physics*, vol. 85, no. 6, p. 905850602, 2019.
- [35] A. Goodman, K. C. Mata, G. Plunk, H. Smith, R. Mackenbach, C. Beidler, and P. Helander, “Constructing precisely quasi-isodynamic magnetic fields,” *Journal of Plasma Physics*, vol. 89, no. 5, p. 905890504, 2023.
- [36] R. Jorge, G. G. Plunk, M. Drevlak, M. Landreman, J.-F. Lobsien, K. C. Mata, and P. Helander, “A single-field-period quasi-isodynamic stellarator,” *Journal of Plasma Physics*, vol. 88, p. 175880504, 2022.
- [37] K. C. Mata, G. G. Plunk, and R. Jorge, “Direct construction of stellarator-symmetric quasi-isodynamic magnetic configurations,” *Journal of Plasma Physics*, vol. 88, p. 905880503, 2022.

- [38] J. R. Cary and S. G. Shasharina, “Omnigenity and quasihelicity in helical plasma confinement systems,” *Physics of Plasmas*, vol. 4, no. 9, pp. 3323–3333, 1997.
- [39] R. Gaur, D. Dudt, R. Conlin, D. Panici, K. Unalmis, and E. Kolemen, “Exploring the database of omnigenous stellarators with DESC,” in *APS Division of Plasma Physics Meeting Abstracts*, vol. 2023 of *APS Meeting Abstracts*, p. AP01.033, Jan. 2023.
- [40] C. Hegna and J. D. Callen, “Stability of bootstrap current-driven magnetic islands in stellarators,” *Physics of plasmas*, vol. 1, no. 9, pp. 3135–3137, 1994.
- [41] M. Landreman and W. Sengupta, “Constructing stellarators with quasisymmetry to high order,” *Journal of Plasma Physics*, vol. 85, no. 6, p. 815850601, 2019.
- [42] E. Sánchez, J. Velasco, I. Calvo, and S. Mulas, “A quasi-isodynamic configuration with good confinement of fast ions at low plasma β ,” *Nuclear Fusion*, vol. 63, no. 6, p. 066037, 2023.
- [43] A. G. Goodman, P. Xanthopoulos, G. G. Plunk, H. Smith, C. Nührenberg, C. D. Beidler, S. A. Henneberg, G. Roberg-Clark, M. Drevlak, and P. Helander, “Quasi-isodynamic stellarators with low turbulence as fusion reactor candidates,” *PRX Energy*, vol. 3, no. 2, p. 023010, 2024.
- [44] A. H. Glasser, “The direct criterion of newcomb for the ideal mhd stability of an axisymmetric toroidal plasma,” *Physics of Plasmas*, vol. 23, p. 072505, 2016.
- [45] A. Glasser, “The DCON3D code for the ideal mhd stability of stepped-pressure stellarators,” in *APS Division of Plasma Physics Meeting Abstracts*, vol. 2020, pp. CP19–016, 2020.
- [46] R. Gaur, *Optimization of High- β Fusion Devices Against Linear Instabilities*. University of Maryland, College Park, 2023.
- [47] G. Acton, M. Barnes, S. Newton, and H. Thienpondt, “Optimisation of gyrokinetic microstability using adjoint methods,” *Journal of Plasma Physics*, vol. 90, p. 905900406, 2024.
- [48] J. Bradbury, R. Frostig, P. Hawkins, M. J. Johnson, C. Leary, D. Maclaurin, G. Necula, A. Paszke, J. VanderPlas, S. Wanderman-Milne, and Q. Zhang, “JAX: composable transformations of Python+NumPy programs,” 2018.
- [49] C. Hegna and S. Hudson, “Ideal magnetohydrodynamic ballooning stability boundaries in three-dimensional equilibria,” *Physics of Plasmas*, vol. 9, pp. 2014–2019, 2002.
- [50] K. Aleynikova and A. Zocco, “Quantitative study of kinetic ballooning mode theory in simple geometry,” *Physics of Plasmas*, vol. 24, no. 9, 2017.
- [51] K. Aleynikova, A. Zocco, P. Xanthopoulos, P. Helander, and C. Nührenberg, “Kinetic ballooning modes in tokamaks and stellarators,” *Journal of Plasma Physics*, vol. 84, p. 745840602, 2018.
- [52] M. B. Villarino, “A note on the accuracy of Ramanujan’s approximate formula for the perimeter of an ellipse,” *Journal of Inequalities in Pure and Applied Mathematics*, vol. 7, no. 1, pp. 1–8, 2006.
- [53] S. Ramanujan, “Modular equations and approximations to π ,” *Quarterly Journal of Mathematics*, vol. 45, pp. 350–372, 1914.
- [54] J. M. Greene, “A brief review of magnetic wells,” *Comments on Plasma Physics and Controlled Fusion*, vol. 17, pp. 389–402, 1997.
- [55] J. Parisi, A. O. Nelson, W. Guttenfelder, R. Gaur, J. W. Berkery, S. M. Kaye, K. K. Barada, C. F. Clauser, A. Diallo, D. R. Hatch, *et al.*, “Stability and transport of gyrokinetic critical pedestals,” *Nuclear Fusion*, 2024.
- [56] M. Kotschenreuther, X. Liu, D. R. Hatch, S. Mahajan, L. Zheng, A. Diallo, R. Groebner, J. C. Hillesheim, C. F. Maggi, C. Giroud, *et al.*, “Gyrokinetic analysis and simulation of pedestals to identify the culprits for energy losses using ‘fingerprints’,” *Nuclear Fusion*, vol. 59, p. 096001, 2019.
- [57] R. P. Feynman, “Space-time approach to quantum electrodynamics,” in *Quantum Electrodynamics*, pp. 178–198, CRC Press, 2018.
- [58] H. Biglari, P. Diamond, and M. Rosenbluth, “Toroidal ion-pressure-gradient-driven drift instabilities and transport revisited,” *Physics of Fluids B: Plasma Physics*, vol. 1, pp. 109–118, 1989.
- [59] W. R. Inc., “Mathematica, Version 14.1.” Champaign, IL, 2024.